**ORIGINAL ARTICLE**

# Computational prediction of surface-tension flow mechanism of molten filler in a V-shaped groove geometry in the brazing process of a heat exchanger

Hiroshi Otsuki[1] · Jun Ishimoto[1] · Naoki Ogasawara[2] · Takumi Abe[3] · Yoshikatsu Nakano[1]

## Abstract

When the temperature rises during the brazing process, only the brazing material melts because of its low melting point. Several analytical approaches have been used to describe filler flow in channels and the progression of erosion grooves. However, only a few studies have examined filler-flow behavior in microgrooves during brazing. In this study, a computational model was constructed to examine the flow in microgrooves on an extruded material's surface. The capillary flow of the aluminum brazing material was numerically analyzed to investigate the physical properties and surface behavior. Specifically, the surface-tension flow behavior was analyzed by simulating various cross-sectional shapes of the channel grooves and various contact angles of the filler. The effects of various parameters, such as viscosity and boundary conditions, on the filler flow were also analyzed. When the cross-sectional area of the channel groove increases, the filler-flow velocity increases, and the rate of unsteady fluctuation increases with the increasing filler tip velocity. The driving force of the filler flow in the channel groove is considered to be (1) the surface tension, which is based on the filler free-surface curvature, or (2) the dynamic change in the shape of the meniscus, which can be unsteady and induced by Rayleigh–Taylor instability. As the cross-sectional area of the channel groove increases, the capillary force based on the dynamic change in meniscus shape dominates the unsteady change in filler tip velocity, rather than the surface tension based on the filler free-surface curvature formed in the groove.

✉ Jun Ishimoto
  ishimoto@alba.ifs.tohoku.ac.jp

  Hiroshi Otsuki
  otsuki.hiroshi.p1@dc.tohoku.ac.jp

  Naoki Ogasawara
  naoki.ogasawara@mahle.com

  Takumi Abe
  abe-takumi@alba.ifs.tohoku.ac.jp

  Yoshikatsu Nakano
  nakano-yoshikatsu@alba.ifs.tohoku.ac.jp

[1] Institute of Fluid Science, Tohoku University, 2-1-1, Katahira, Aoba-Ku, Sendai 980–8577, Japan

[2] MAHLE Japan Limited, 1-480 Inuzuka, Oyama, Tochigi 323-8678, Japan

[3] TDK Corporation, Nihonbashi Takashimaya Mitsui Building, 2-5-1, Nihonbashi, Chuo-Ku, Tokyo 103-6128, Japan

## 1 Introduction

### 1.1 Erosion grooves in heat exchangers

Aluminum alloy heat exchangers for automotive applications comprise a header that serves as the inlet/outlet for refrigerant, flat tubes that serve as the flow path of the refrigerant, and corrugated fins that improve heat exchange. These parts are generally assembled by brazing, joining the parts using a molten filler material. Specifically, after the tubes and fins are laminated in layers, the tube ends are inserted into the header slot holes, fixed with a jig, and then heated and cooled in a furnace to complete the controlled-atmosphere brazing process [1–3].

A common aluminum alloy material used for brazing is known as a brazing sheet, comprising a core of aluminum alloy clad with a thin layer of Al-Si. When the temperature rises, only the Al-Si alloy layer melts because of its low melting point [4–9], and it flows into the joints to fill the

gaps between the parts, where it solidifies upon cooling, completing the brazing process.

The aluminum alloy substrate is dissolved by the liquid filler to some extent. It is considered an "erosion groove" when a large amount of liquid filler flows and dissolves a substrate enough to form grooves in it [10–12]. The formation of erosion grooves is one of the most severe problems that can occur in the brazing process, when melting the filler causes partial loss of the aluminum base [11, 13–15]. If the base material deteriorates and the base is penetrated, the product is regarded as defective. Even without penetration, the product lifetime is shortened, and the heat exchanger may cease to function if refrigerant leaks through a hole in one of its parts.

Figures 1 and 2 show an example of erosion grooves on an extruded tube inserted into a header component. Before brazing, there are linear microgrooves with a depth of approximately 10 μm on the surface of the tube, aligned in the extrusion direction. During brazing, erosion grooves are produced by the selective flow of the header's molten filler through the microgrooves.

Erosion grooves are generally caused near the melting point of the filler material, either by the melting of the Al alloy matrix or by grain boundary penetration by the Al-Si filler. The factors that influence this phenomenon include the type of filler material, the type of base metal, temperature, and the shape of the groove. The effects of various factors (e.g., Si concentration of the brazing sheet and temperature) on erosion have been reported for simple shapes [16, 17].

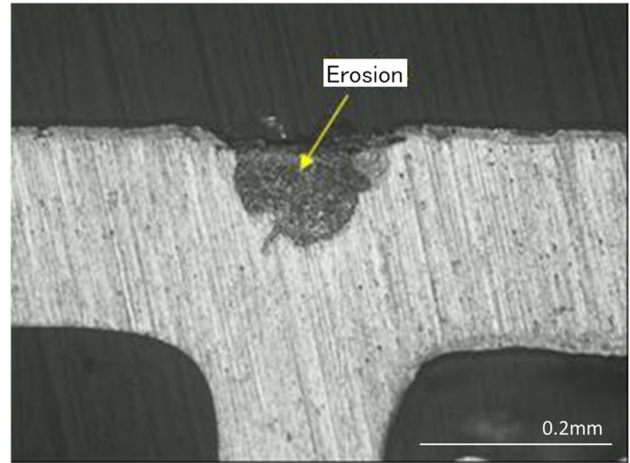The degree of erosion has been compared between continuous filler flow in a channel groove (i.e., a gutter for



**Fig. 2** Cross section of an eroded extruded tube

filler flow) and the case where the filler stays in the channel groove, showing that continuous filler flow results in considerably increased erosion. Therefore, it is necessary to clarify how the filler flow behaves, to enhance the flow characteristics while mitigating the progression of erosion grooves [18].

This study focuses on the flow of molten filler in microgrooves. To date, few analytical approaches have been used to understand filler flow in channels and the progression of erosion grooves, and few studies have been conducted to elucidate the mechanisms of filler-flow phenomena. In this study, an analytical model was developed for examining flow in microgrooves on the surface of an extruded material, and the capillary flow behavior of the aluminum brazing material was numerically analyzed.

**Fig. 1** Overview of an extrusion tube surface before and after brazing. Before brazing, the surface has a roughness of approximately 10 μm; after brazing, erosion grooves appear where the roughness was large before brazing
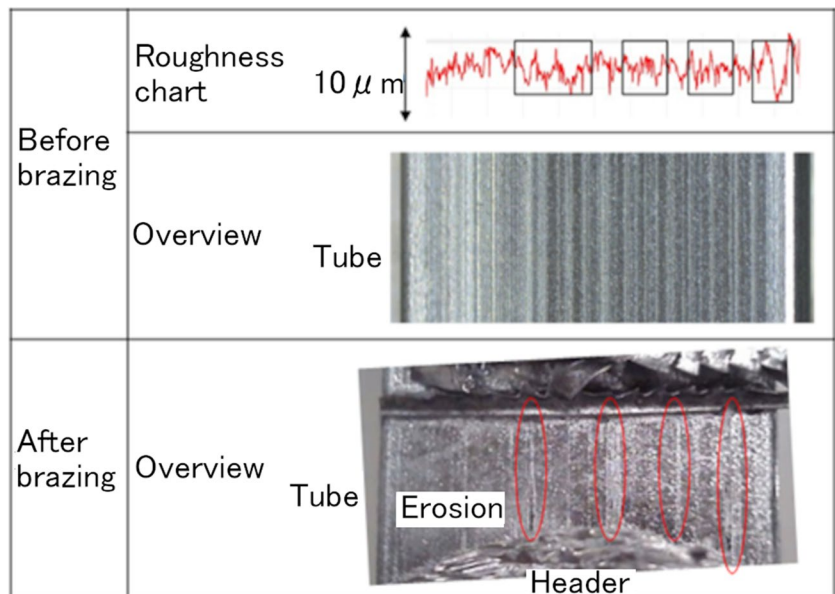
## 1.2 Surface tension and contact angle in aluminum brazing

In aluminum brazing, molten filler flows into the joints between parts by capillary action, and the associated surface tension and contact angle are governed by Young's equation. Considering its contact angle, the aluminum filler exhibits good wettability, as shown in work on the predicted shape of joint filet formation, where a contact angle of 0° was used [19–25].

However, obtaining the actual surface tension and contact angle of the filler is considered difficult for the following three reasons [26–31]. (1) The presence of an aluminum oxide film and flux solution is an obstacle to evaluating the surface tension. (2) The amounts of Si and Cu in an aluminum alloy affect the surface tension of the brazing material, and the addition of Bi, Ca, Li, Mg, Pb, and Sb has been reported to lower the surface tension of the brazing material. (3) The surface tension of an aluminum alloy liquid is correlated with temperature: as the temperature increases, the surface tension tends to decrease (i.e., the higher the temperature, the greater the brazing wettability).

## 1.3 Capillary flow between flat plates

When two glass plates are placed vertically in a fluid, like water, with a gap between them, the fluid rises to the top of the plates when the gap is sufficiently narrow but does not rise when it is too wide. This capillary phenomenon occurs in numerous cases, including filler flow.

The smaller the gap between parts, the greater the penetration distance and velocity associated with the capillary force (equivalent to the capillary pressure), suggesting that the filler-flow behavior also depends on the channel geometry, designated as surface-tension flow through microgrooves in the present study [29].

## 2 Numerical model

### 2.1 Computational modeling

To analyze the surface-tension flow behavior of the molten brazing material in a microgroove geometry, a two-phase fluid comprising air and molten filler material was used as the working fluid. In the case of the capillary flow in a V-shaped groove, which is the subject of this study, the formation of small turbulent eddies induced by surface-tension flow, especially in the early stages of flow, is the dominant factor in the overall unsteady flow. It is necessary to analyze the formation of the initial turbulent eddies accurately. Herein, a

high-resolution Smagorinsky-type large eddy simulation (LES) was employed. Furthermore, the volume of fluid (VOF) method [32–36] was used to capture the capillary interface.

To compute the present system, an original computational fluid dynamics solver was developed using the open-source finite volume code from OpenFOAM based on the extended form of *interFoam*. This customized solver, named *FillerCapillaryFoam*, can be used to calculate the capillary flow of molten filler in the surface-tension model. The computational time for each case accompanied by 128-core parallel computing is approximately 15 h.

The validation of this calculation is currently underway using a simple experimental apparatus with a V-shaped groove to measure surface-tension flow using micro-PIV, and a follow-up report is planned.

### 2.2 Basic equations

The governing equations are given below, Eqs. 1, 2, 3, 4, 5, 6, 7, and 8,

Equation of continuity:

$$\frac{\partial \rho}{\partial t} + \nabla \cdot (\rho \boldsymbol{U}) = 0 \tag{1}$$

Momentum equation:

$$\frac{\frac{\partial \rho \boldsymbol{U}}{\partial t} + \nabla \cdot (\rho \boldsymbol{U}\boldsymbol{U})}{= -\nabla P + \nabla \cdot \boldsymbol{\tau} + \rho \boldsymbol{g} + \boldsymbol{F}_s} \tag{2}$$

Body force calculated from surface tension (CSF model):

$$\boldsymbol{F}_s = \sigma k \nabla \alpha = -\sigma \nabla \cdot \left(\frac{\nabla \alpha}{|\nabla \alpha|}\right) \nabla \alpha \tag{3}$$

where $\rho$ is density, $\mathbf{U}$ is the flow velocity vector, $\tau$ is the viscous stress tensor, $P$ is absolute pressure, and $\mathbf{g}$ is the gravitational acceleration vector. The $\mathbf{F}_S$ term in the equation of motion replaces the surface tension with a body force, in accordance with the CSF model.

The interface between the phases is simultaneously computed using a surface-capturing methodology, which employs the volume fraction of one of the phases as an indicator function, called the VOF, to identify the different fluids. The interface is not defined as a sharp boundary. Instead, a transition region is created where the fluid is treated as a mixture of the two fluids on each side of the interface, which is a discontinuous step in reality. The indicator function is equivalent to the liquid-phase volume fraction α. When the interface is

**Table 1** Fluid properties

| Fluid | Kinematic viscosity (m$^2$/s) | Density (kg/m$^3$) |
|---|---|---|
| Melted filler | $6.62249 \times 10^{-6}$ | 2490 |
| Air | $1.604 \times 10^{-5}$ | 1.165 |

**Table 2** Surface tension

| Combination | Surface tension (kg/s$^2$) |
|---|---|
| Melted filler + air | $941 \times 10^{-3}$ |

**Table 3** Boundary conditions

| Surface condition | Velocity boundary condition | Pressure boundary condition |
|---|---|---|
| Wall | Zero velocity (no slip) | Zero gradient |
| Surface | Function with backflow | Total pressure |

**Table 4** Dimensions of flow-channel groove shape

| Case no | Width $h_w$ (μm) | Depth $h_d$ (μm) |
|---|---|---|
| 14 | 10 | 5 |
| 15 | 50 | 5 |
| 16 | 80 | 5 |
| 18 | 100 | 10 |
| 19 | 10 | 2 |
| 20 | 100 | 20 |

the subgrid scale on the resolved eddies in Eq. 2 is represented by the sub grid scale stress because it represents the effect of the unresolved small-scale turbulence.
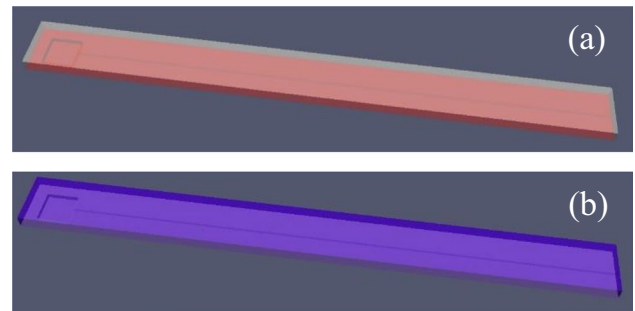


**Fig. 3** Computational geometry. **a** Boundary at the bottom of the computational domain. **b** Boundary at the top of the computational domain

advected by the flow, the evolution of the VOF advection equation, that is, the transport equation of the volume fraction α, is given by the following conservation equation:

VOF transport equation:

$$\frac{\partial \alpha}{\partial t} + \nabla \cdot (U\alpha) = 0 \tag{4}$$

$$\rho = \alpha \rho_l + (1 - \alpha)\rho_g \tag{5}$$

$$\mu = \alpha \mu_l + (1 - \alpha)\mu_g \tag{6}$$

$$\mu^{eff} = \mu + \mu \prime \tag{7}$$

$$\tau = \nabla \cdot \left\{ \mu^{eff} \left( \nabla U + \nabla U^T - \frac{2}{3}I\nabla \cdot U \right) \right\} \tag{8}$$

where subscript $l$ is the liquid phase, and $g$ is the gas phase.

The LES-VOF equations are derived from Eq. 2 through a localized volume averaging of the phase-weighted properties. This process is more commonly known as filtering because it removes the microscopic scales of motion from the direct calculation. This averaging, in conjunction with the non-linear convection term in Eq. 2, produces an additional quantity in the momentum equation that cannot be directly calculated. The effect of
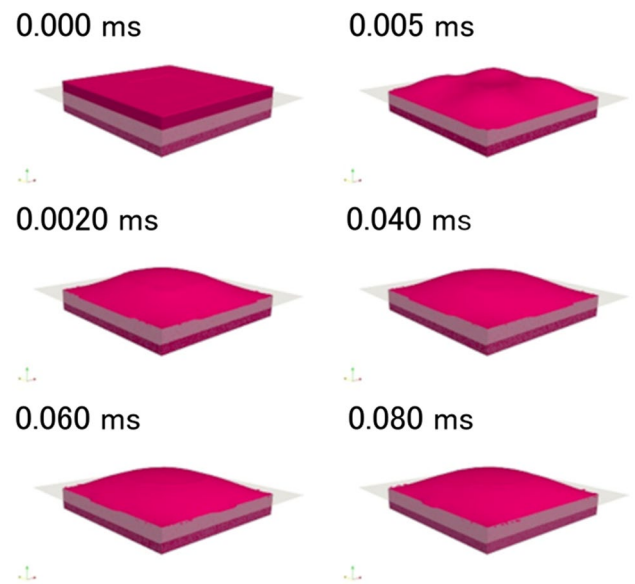


**Fig. 4** Instantaneous shape of the filler meniscus

## 2.3 Calculation conditions

The model comprised (i) a pool of molten filler and (ii) a channel groove, and the filler-flow characteristics in the channel groove were analyzed. The physical properties and numerical conditions are listed in Tables 1, 2, and 3. Table 4 gives the dimensions of the channel groove shape. The flow behavior was analyzed for six microscale V-shaped channel geometries, with different widths $h_w$ and depths $h_d$.
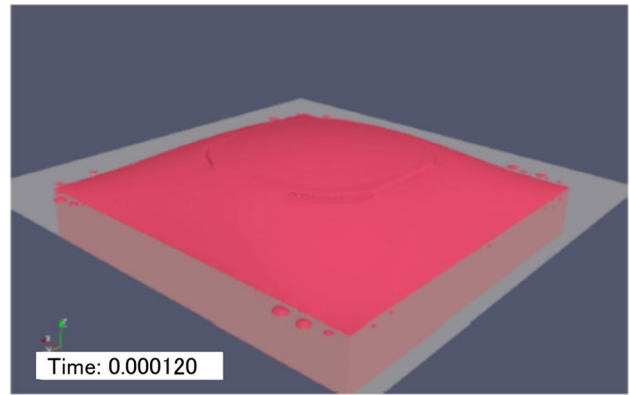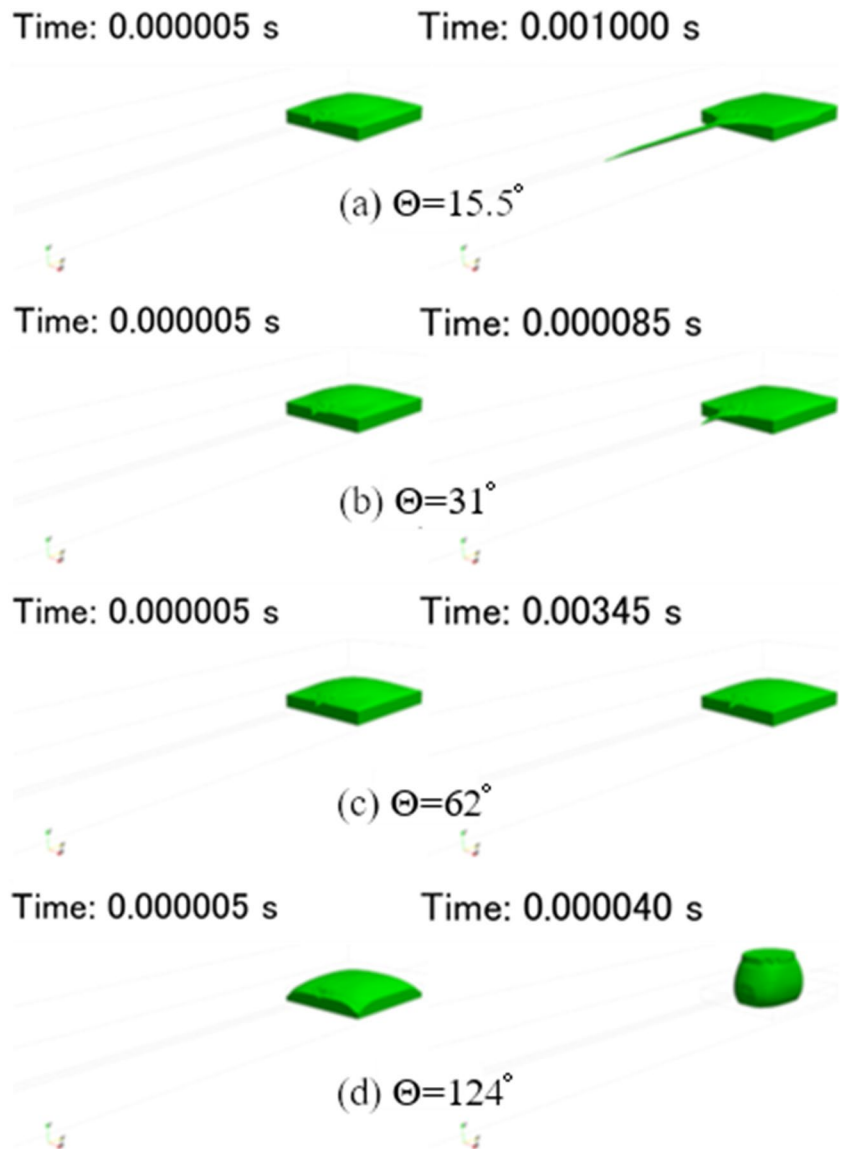


Time: 0.000120

**Fig. 5** Meniscus shape of a molten filler pool

**Fig. 6** Flow in channel groove no. 14 ($\theta_C = 15.5°$, 31°, 62°, and 124°)



Time: 0.000005 s          Time: 0.001000 s

(a) $\Theta = 15.5°$

Time: 0.000005 s          Time: 0.000085 s

(b) $\Theta = 31°$

Time: 0.000005 s          Time: 0.00345 s

(c) $\Theta = 62°$

Time: 0.000005 s          Time: 0.000040 s

(d) $\Theta = 124°$

# 3 Influence of initial meniscus shape

## 3.1 Investigation of flow driving force

Capillary flow is affected by gravity and surface tension. The effect of gravity is evaluated using the capillary length $l_0$, which is expressed in Eq. 9:

$$l_0 = \sqrt{\frac{\gamma}{\rho g}} \qquad (9)$$

where $\gamma$ is surface tension, $\rho$ is density, and $g$ is the acceleration due to gravity. In the present study, we have $\gamma = 0.941$ N/m, $\rho = 2490$ kg/m$^3$, and $g = 9.81$ m/s$^2$, resulting in a capillary length of 6.2 mm. The values of these properties are based on our physical measurements. The scale of the meniscus is 5 mm in length and width and 0.5 mm in depth for large sizes, indicating that this phenomenon involves flow in which surface tension is dominant.

In the numerical calculations, it was difficult to separate the individual phenomena because the formation of the meniscus in the brazing pool and the flow of the molten filler in the channel groove coincided with the initial conditions. Therefore, we decided to numerically analyze the filler flow in the channel groove after the meniscus shape becomes stable.

## 3.2 Results for the initial meniscus condition

We constructed a heat exchanger's filler flow model that assumes a microscale groove on a tube and a header's melted filler. The model geometry was limited to the molten pool and then the meniscus formation behavior was numerically calculated (Fig. 3). However, the filler
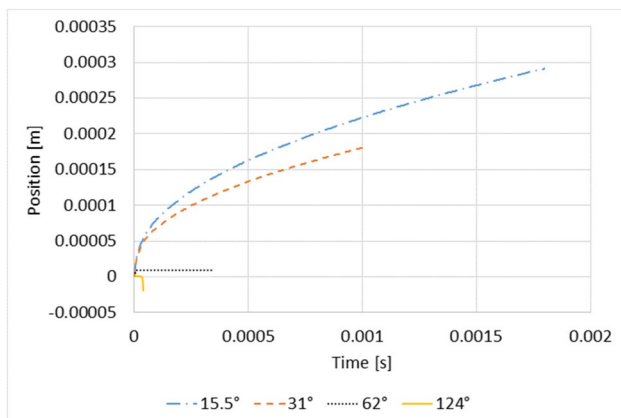


**Fig. 7** Filler tip position of a flow in channel groove no. 14 ($\theta_C = 15.5°$, 31°, 62°, and 124°)
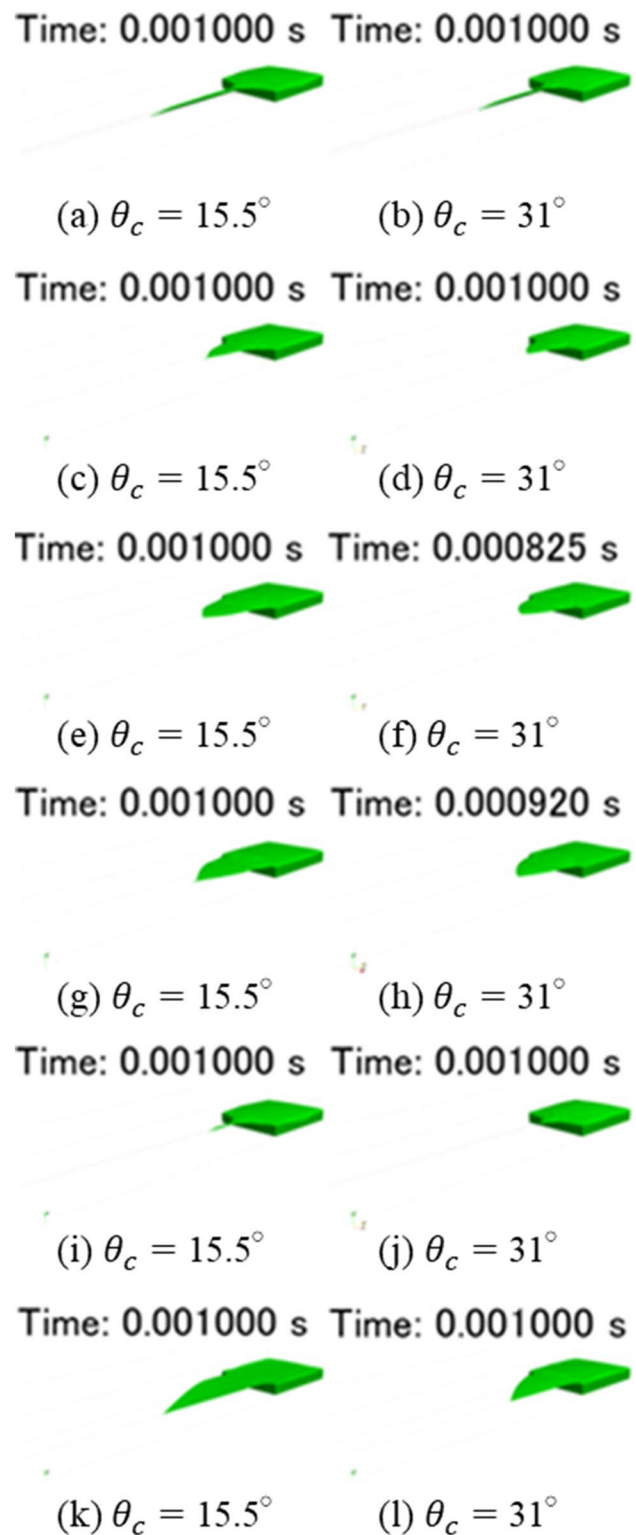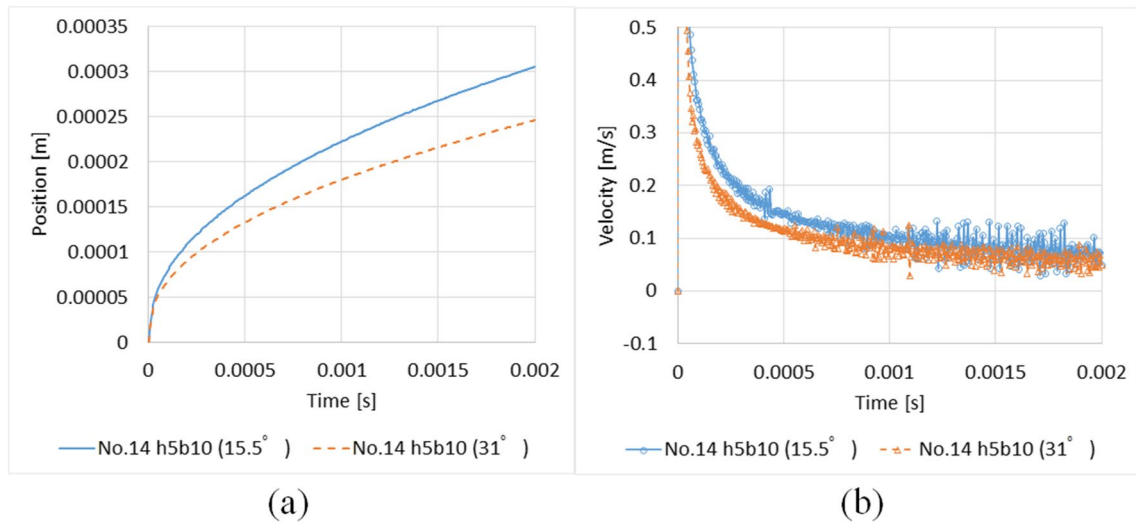


**Fig. 8** Instantaneous filler flow in the channel grooves. **a, b** Channel groove no. 14. **c, d** Channel groove no. 15. **e, f** Channel groove no. 16. **g, h** Channel groove no. 18. **i, j** Channel groove no. 19. **k, l** Channel groove no. 20
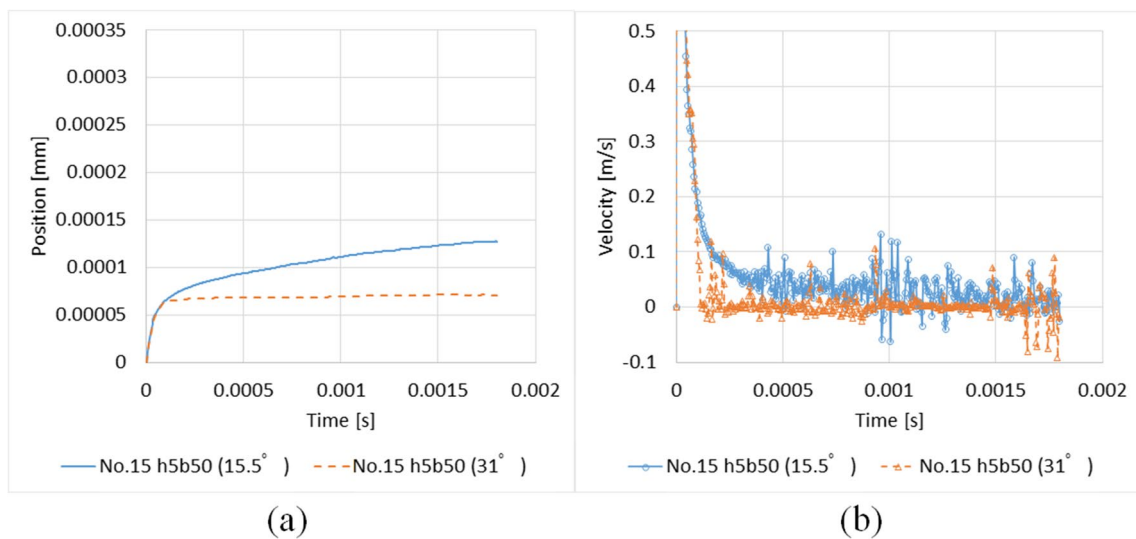
**Fig. 9** Flow in channel groove no. 14 (contact-angle comparison $\theta_c$). **a** Filler tip position. **b** Filler tip velocity

flows as it melts; it is not pooled. Therefore, we aimed to calculate the filler flow in a microgroove without pooling by studying the instantaneous shape of the filler meniscus, as shown in Fig. 4. The pooled box-shaped filler forms a stable meniscus shape while changing its shape according to the dam-break model. Figure 5 shows the meniscus shape of a pool of molten filler. This stable shape was used as the initial condition to reduce the influence of changes in the shape of the meniscus of the molten filler on the filler flow in the groove.

## 4 Results and discussion

### 4.1 Differences in flow characteristics due to contact angle ($\theta_c = 15.5$–124°)

Figure 6 shows the filler-flow behavior in the channel grooves when the contact angle $\theta_c$ was 15.5°, 31°, 62°, and 124°, and Fig. 7 shows the filler tip position in the channel grooves for the same angles.



**Fig. 10** Flow in channel groove no. 15 (contact-angle comparison $\theta_c$). **a** Filler tip position. **b** Filler tip velocity
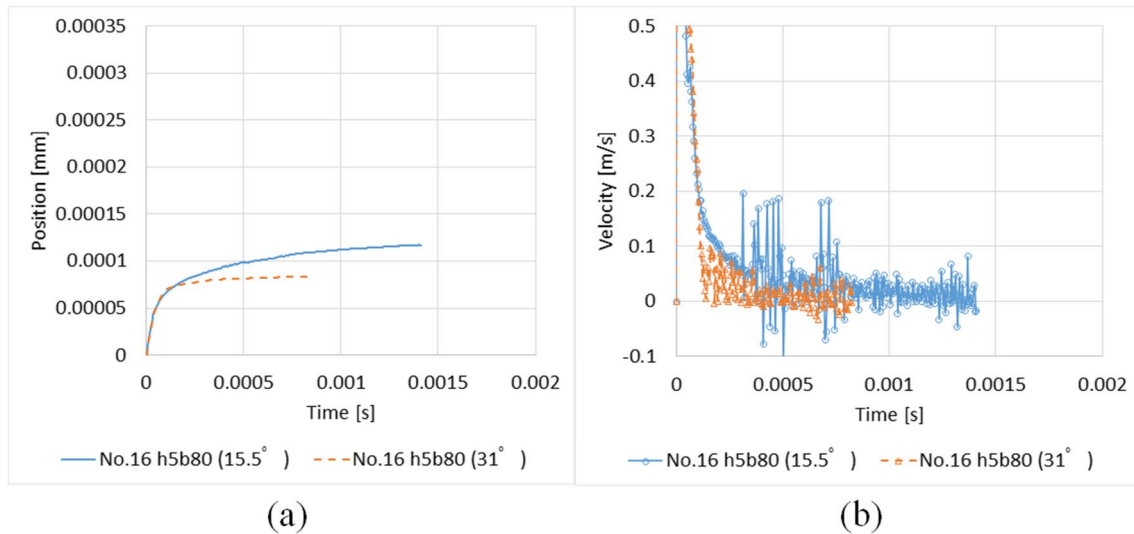
**Fig. 11** Flow in channel groove no. 16 (contact-angle comparison $\theta_c$). **a** Filler tip position. **b** Filler tip velocity

Considering the filler tip position for $\theta_c = 15.5°$ and $31°$, the filler fluid movement is reduced for $\theta_c = 31°$ compared with that for $\theta_c = 15°$. At a contact angle of $62°$, a small amount of filler fluid initially flowed from the pool into the channel groove, but the flow in the direction of the empty channel stopped almost immediately. At a contact angle of $124°$, the filler did not flow into the channel groove at all, and the filler gathered in the pool.

Therefore, to generate filler flow in microgrooves, the contact angle of the molten filler with the channel wall must be below a certain level for the surface tension acting in the groove to dominate.

To clarify the flow behavior of the filler in the grooves, numerical calculations were performed under the conditions of $\theta_c = 15.5°$ and $31°$.

## 4.2 Differences in flow characteristics due to contact angle (comparison of $\theta_c = 15.5°$ and 31°)

Figure 8 shows the instantaneous behavior of the molten filler in each microgroove shape, and Figs. 9, 10, 11, 12, 13, and 14 show comparisons of the time variations of the
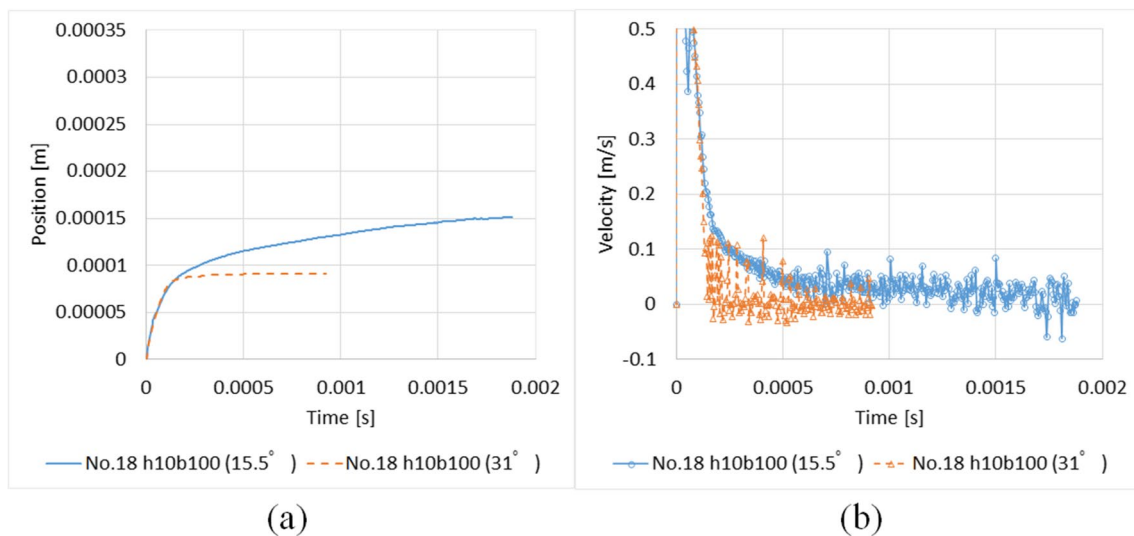


**Fig. 12** Flow in channel groove no. 18 (contact-angle comparison $\theta_c$). **a** Filler tip position. **b** Filler tip velocity
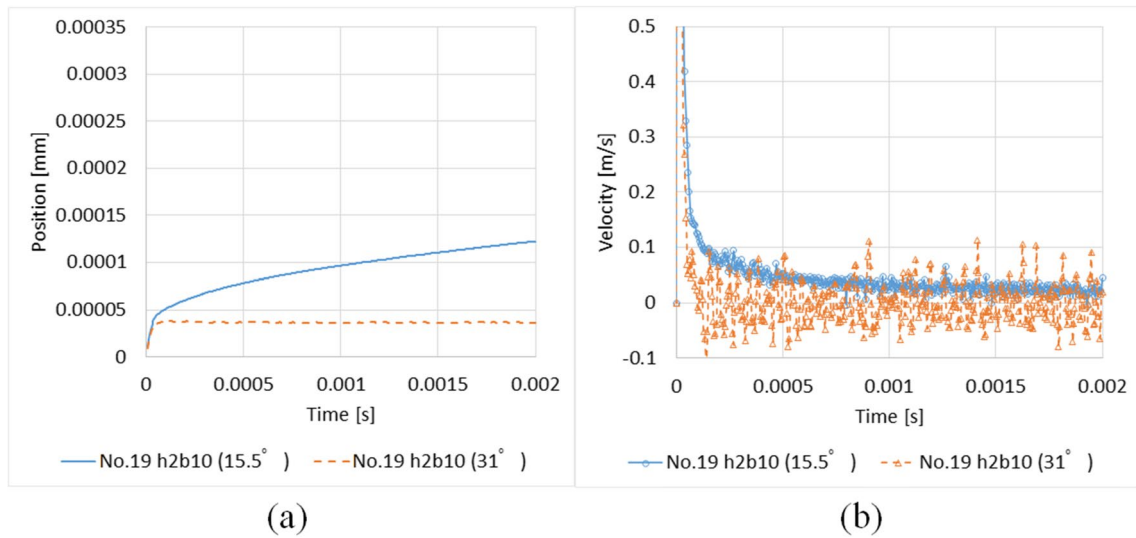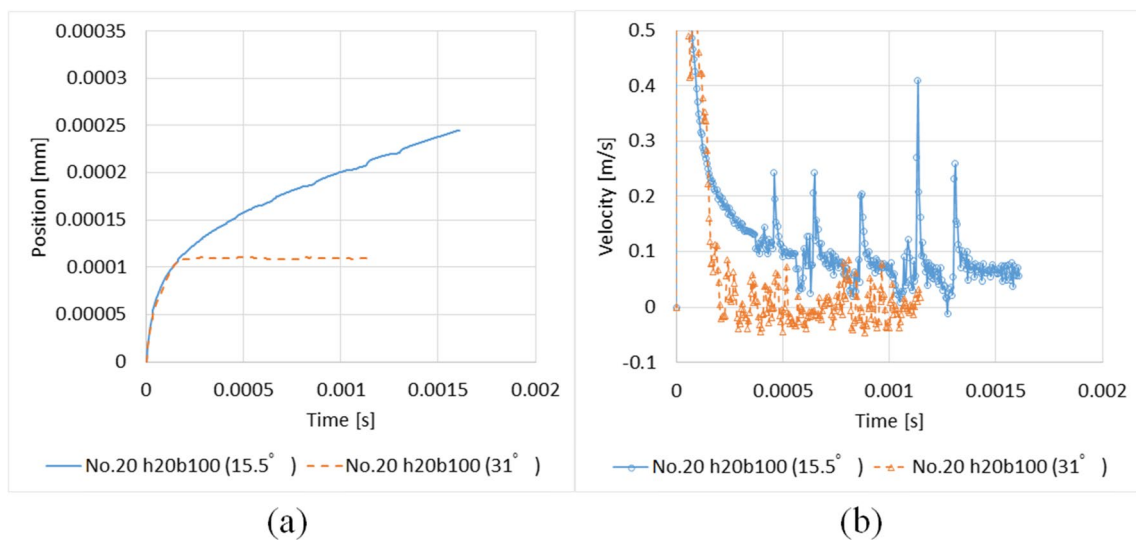
**Fig. 13** Flow in channel groove no. 19 (contact-angle comparison $\theta_c$). **a** Filler tip position. **b** Filler tip velocity

filler tip position and velocity, depending on the contact angle, for each cross-sectional groove size.

In all the channel grooves, surface-tension flow was observed under $\theta_c = 15.5°$. The filler flow was also observed in channel groove no. 14 at a contact angle of 31°, and it was found that the filler fluid velocity increased with decreasing contact angle. In the other channels (channel nos. 15, 16, 18, 19, and 20), the filler flow stopped abruptly at $\theta_c = 31°$, and the filler tip velocity became zero. Even in the case of sudden cessation, the movement distance before cessation differed depending on the channel groove shape. This may be because, when

the contact angle is small, the surface tension acting on the groove is more substantial than that acting on the brazing pool, whereas when the contact angle is large, the surface tension acting on the brazing pool is more substantial. We then examined the surface tension flow's dependence on the channel groove location.

Figure 15 shows enlarged images of the filler tip in each channel groove for the $\theta_c = 15.5°$ condition. The filler tip has an acute angle near the bottom of the channel groove, indicating that the filler flowed first at the bottom. This indicates that the surface-tension flow behavior differs depending on the location in the channel



**Fig. 14** Flow in channel groove no. 20 (contact-angle comparison $\theta_c$). **a** Filler tip position. **b** Filler tip velocity

**Fig. 15** Enlarged filler tip in the channel ($\theta_c = 15.5°$, $t = 0.001$ s). **a** Channel groove no. 14. **b** Channel groove no. 15. **c** Channel groove no. 16. **d** Channel groove no. 18. **e** Channel groove no. 19. **f** Channel groove no. 20

(a) Channel groove no. 14

(b) Channel groove no. 15

(c) Channel groove no. 16

(d) Channel groove no. 18

(e) Channel groove no. 19

(f) Channel groove no. 20

(a)

(b)
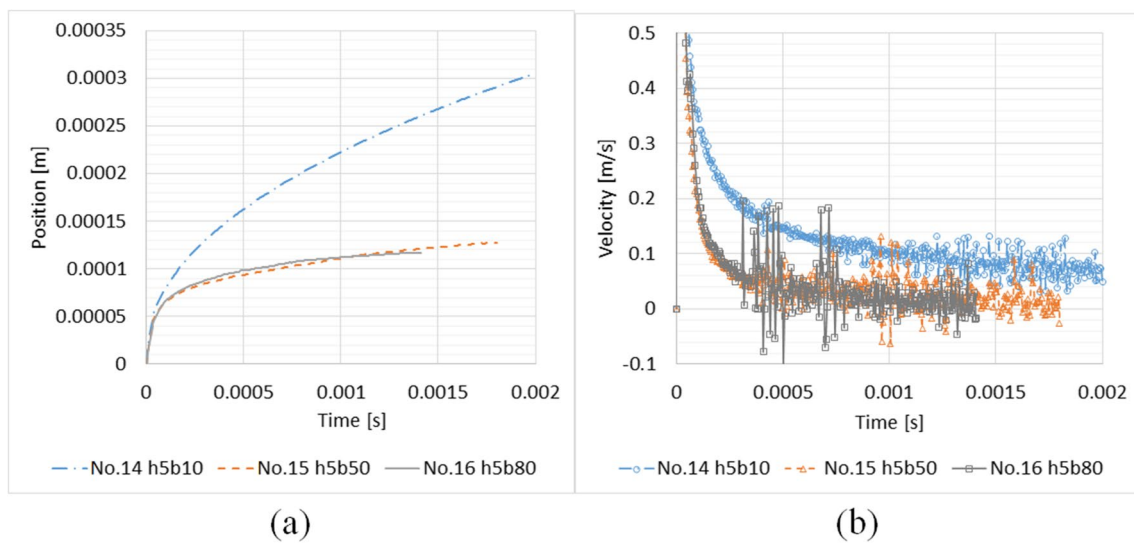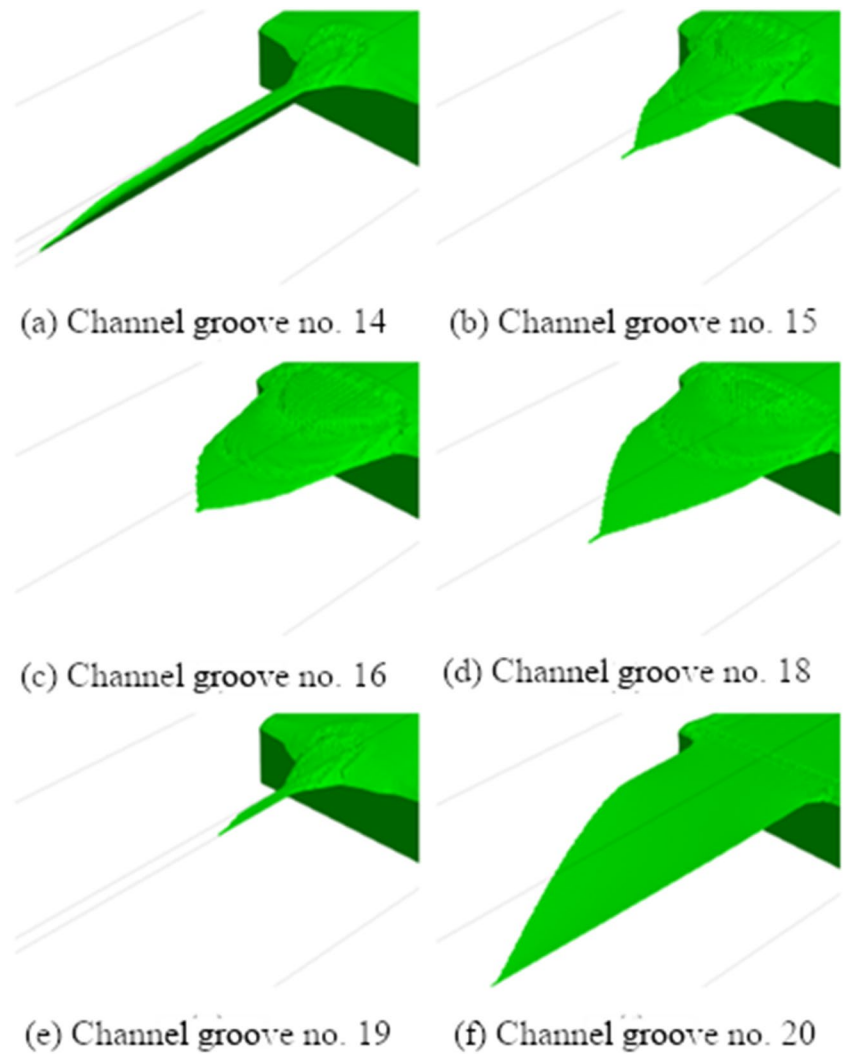
**Fig. 16** **a** Filler tip position. **b** Filler tip velocity (width comparison; $\theta_c = 15.5°$, $h_d = 5$ μm)
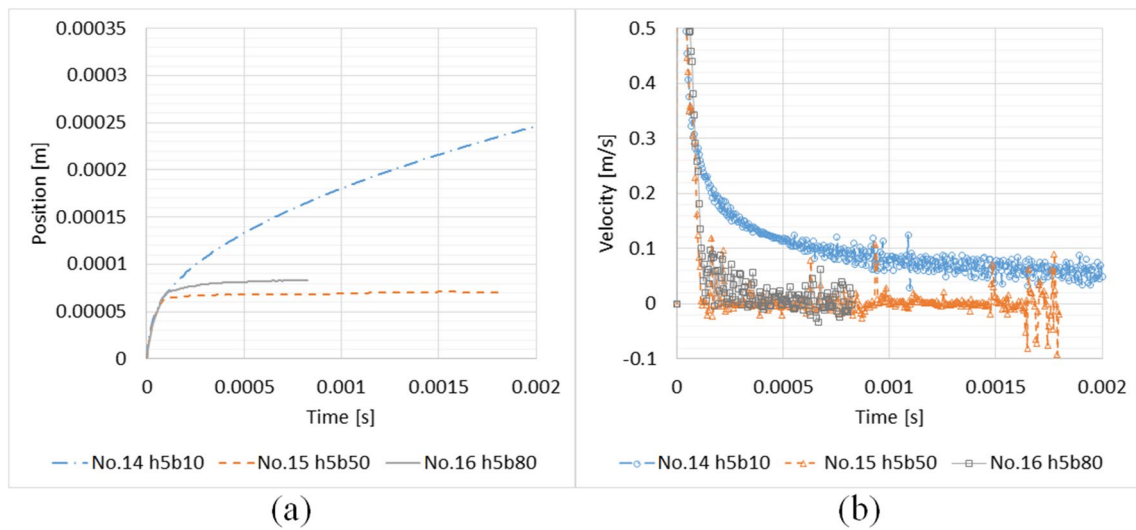
**Fig. 17** **a** Filler tip position. **b** Filler tip velocity (width comparison; $\theta_c = 31°$, $h_d = 5$ μm)

groove. In particular, the capillary force increased near the bottom of the channel groove.

The fact that filler flow was observed In some channel grooves and suppressed in others under the same contact-angle conditions suggests that the geometry of the channel grooves affects the filler flow. Therefore, we compared the filler flow of the channel grooves in terms of the channel width, depth, and cross-sectional area.

### 4.3 Differences in flow due to cross-sectional dimensions

#### 4.3.1 Differences due to groove width

Figures 16 and 17 show comparisons of the filler tip position and filler tip velocity with respect to time, where the depth of the cross-sectional groove dimensions and the contact conditions is the same, and only the width of the channel groove differs.
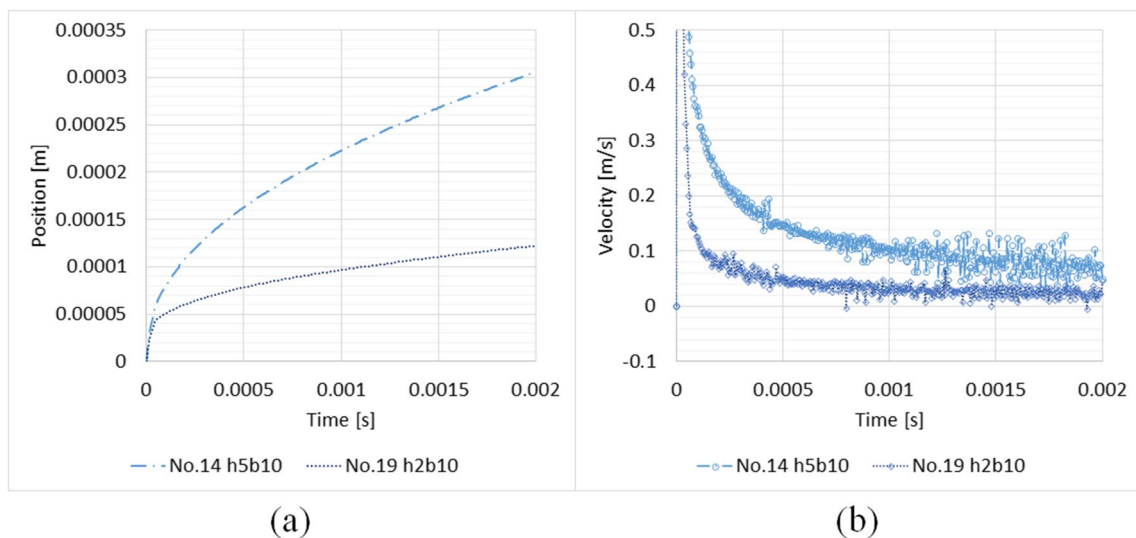


**Fig. 18** **a** Filler tip position. **b** Filler tip velocity (depth comparison; $\theta_c = 15.5°$, $h_w = 10$ μm)
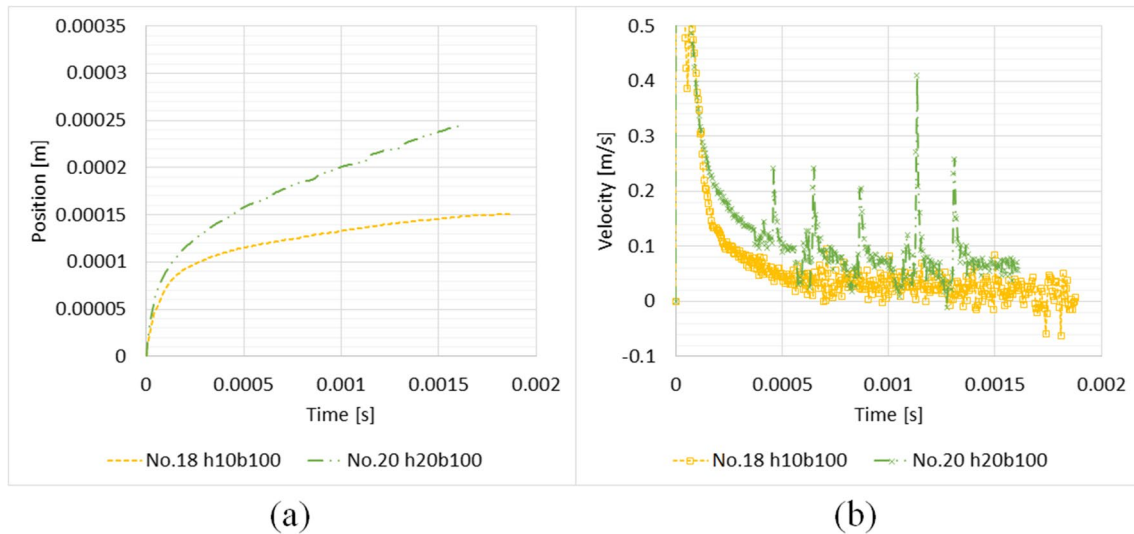
**Fig. 19** **a** Filler tip position. **b** Filler tip velocity (depth comparison; $\theta_c = 15.5°$, $h_w = 100$ μm)

The filler-flow velocity increased with the decreasing width of the channel groove for both contact conditions ($\theta_c = 15.5°$ or 31°). The surface curvature of the filler increased as the channel width decreased, while the groove depth was fixed. As the width of the channel groove decreased, the capillary force increased, as did the filler tip velocity.

### 4.3.2 Difference due to groove depth

Figures 18, 19, 20, and 21 show comparisons of the filler tip position and velocity, where the width of the cross-sectional groove dimensions and the contact conditions is the same, and only the depth of the channel groove differs.

For all contact conditions ($\theta_c = 15.5°$ or 31°) and groove widths ($h_w = 10$ or 100 μm), it was found that the filler-flow velocity increased with the increasing depth of the channel groove. Furthermore, the surface curvature of the filler fluid increased for the larger groove depths with the same groove widths, increasing the filler fluid tip velocity in the deeper groove.

### 4.3.3 Difference due to groove cross-sectional area

Figures 22 and 23 show comparisons of the filler tip position and velocity for the same contact conditions and the same width-to-depth ratio of the cross-sectional groove dimensions, and only the cross-sectional area of the channel groove differs.
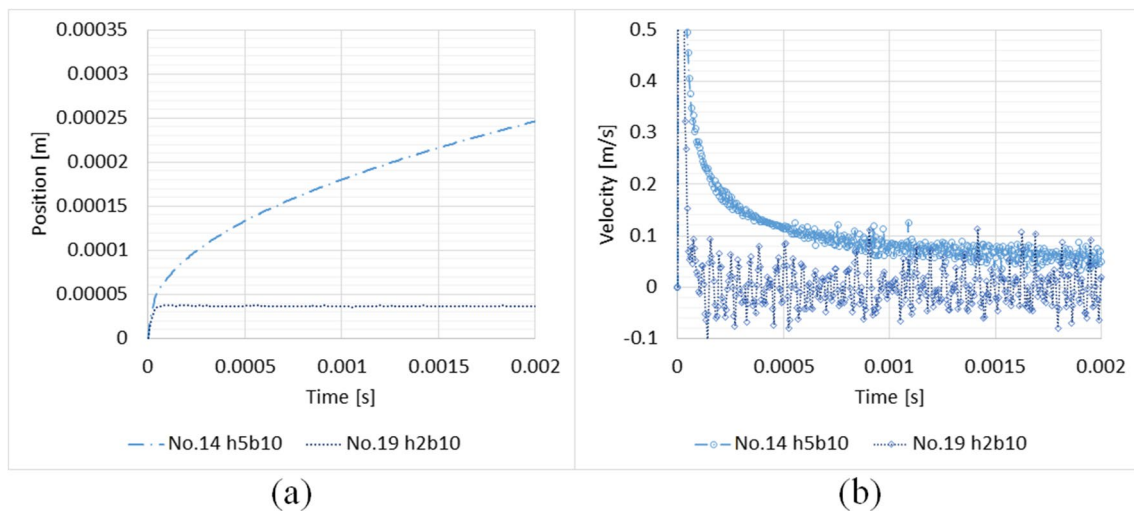


**Fig. 20** **a** Filler tip position. **b** Filler tip velocity (depth comparison; $\theta_c = 31°$, $h_w = 10$ μm)
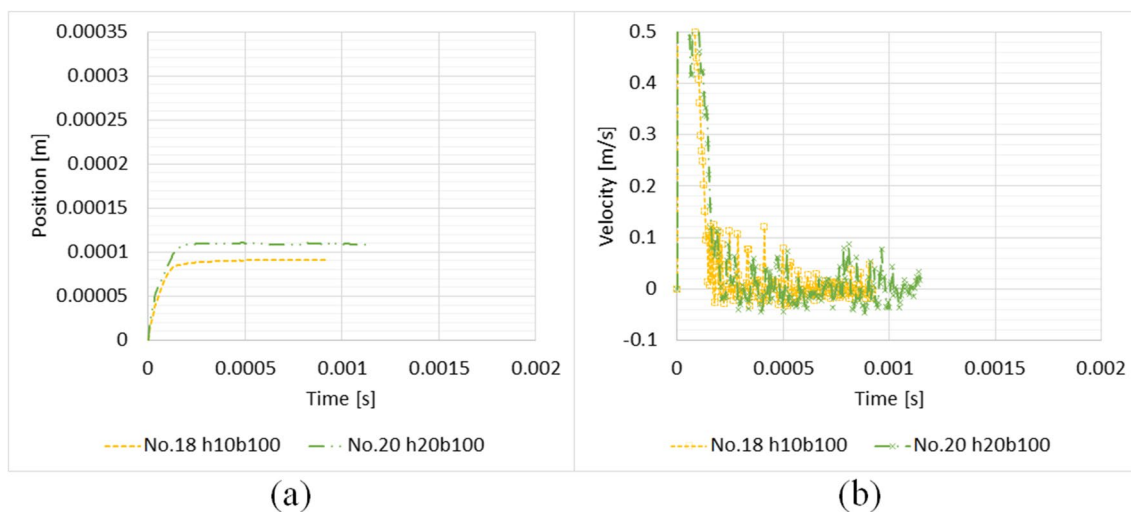
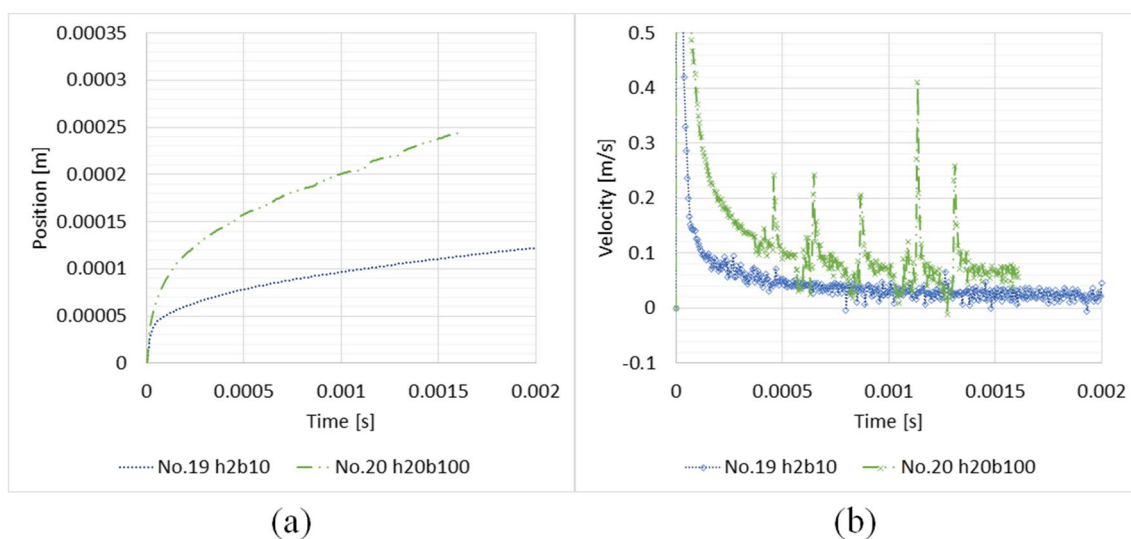**Fig. 21** **a** Filler tip position. **b** Filler tip velocity (depth comparison; $\theta_c = 31°$, $h_w = 100$ μm)

The filler-flow velocity increased with a larger cross-sectional area under all contact conditions. The results for the filler tip velocity under a contact angle of 15° show an unsteady spike-like increase in velocity for the larger cross-sectional area.

The driving force of the filler flow is considered to be the surface tension based on the initial meniscus shape formed when the fluid flows into the groove or the dynamic change in the shape of the meniscus formed when the fluid flows in the groove. The change in meniscus shape at the gas–liquid interface is considered to be induced by Rayleigh–Taylor instability, a phenomenon in which the curvature of the gas–liquid interface changes unstably when the high-density fluid flows into the low-density gas [37]. Herein, the scale modeling results based on the capillary length indicate that the effect of gravity on the brazing fluid is negligible.

The unsteady increase in the filler tip velocity indicates that the change in the dynamic meniscus shape is the driving force for the surface-tension flow in the groove. As the cross-sectional area of the channel groove increases, the capillary force based on the dynamic change in meniscus shape in the flowing state in the groove dominates the unsteady change in filler tip velocity, rather than the surface tension based on the filler free-surface curvature formed in the groove.



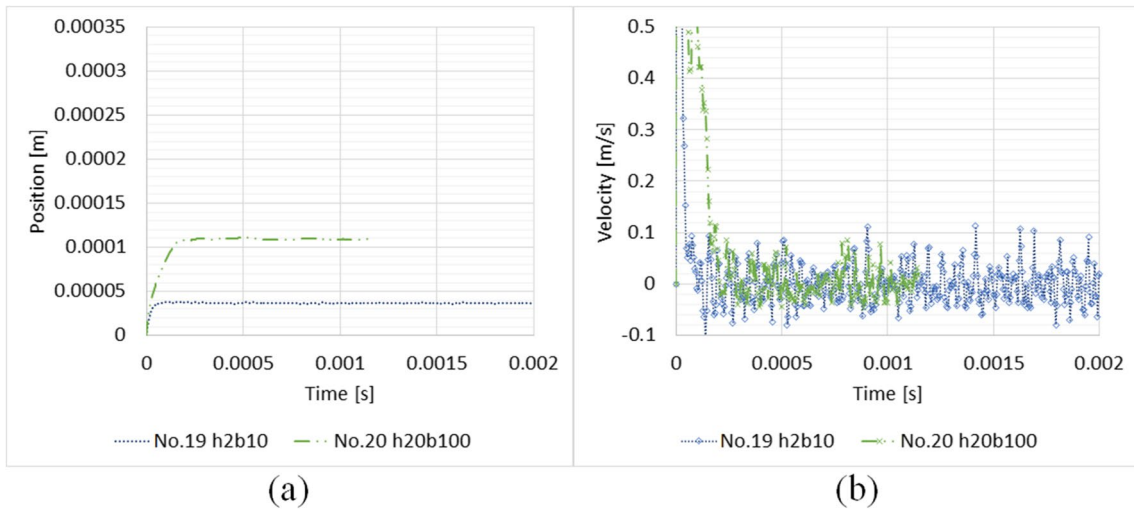**Fig. 22** **a** Filler tip position. **b** Filler tip velocity (size comparison; $\theta_c = 15°$)

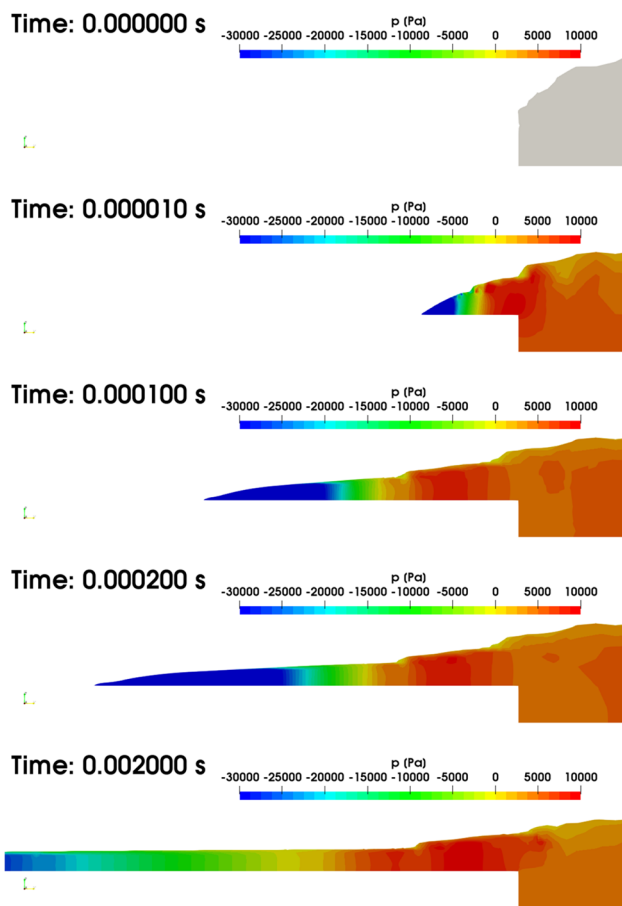**Fig. 23** **a** Filler tip position. **b** Filler tip velocity (size comparison; $\theta_c = 31°$)



**Fig. 24** Pressure distribution of filler flow ($\theta_c = 15.5°$; channel groove no. 14; $t = 0$, $1.0 \times 10^{-5}$ s, $1.0 \times 10^{-4}$ s, $2.0 \times 10^{-4}$ s, and $2.0 \times 10^{-3}$ s)
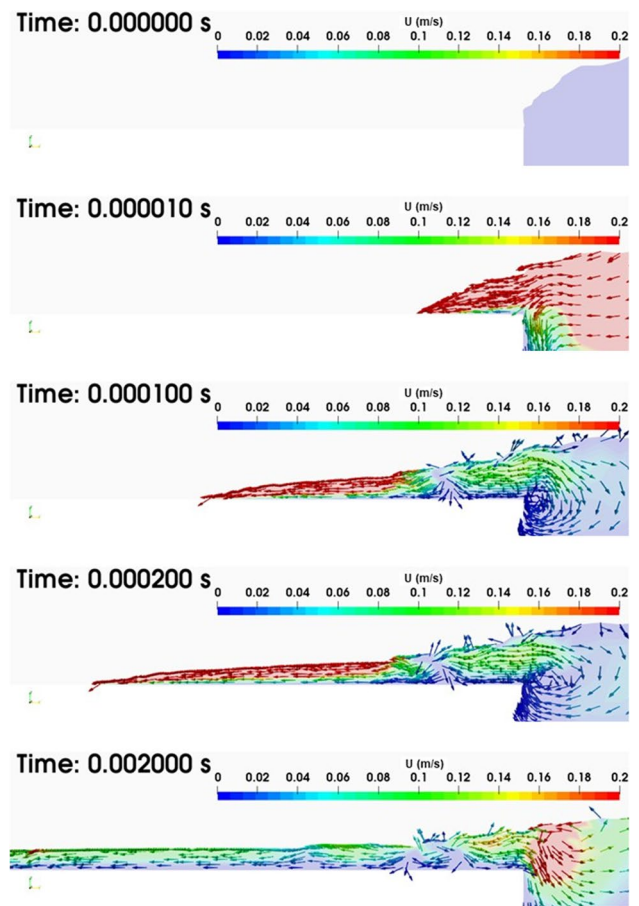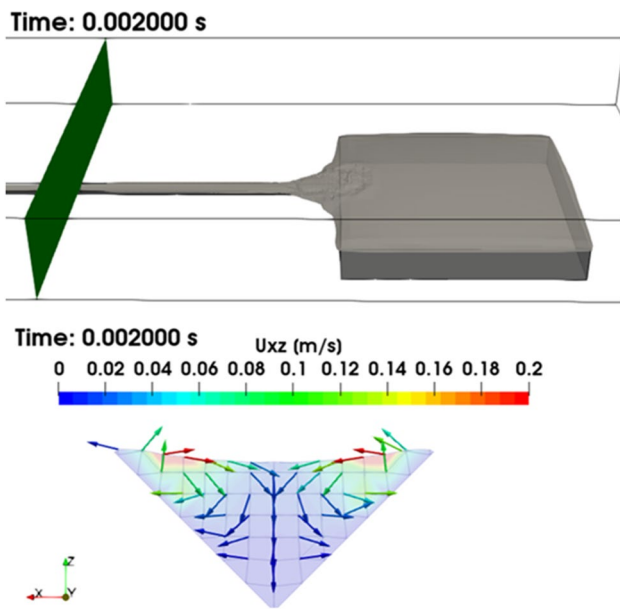
**Fig. 25** Velocity distribution of filler flow ($\theta_c = 15.5°$; channel groove no. 14, $t = 0$, $1.0 \times 10^{-5}$ s, $1.0 \times 10^{-4}$ s, $2.0 \times 10^{-4}$ s, $2.0 \times 10^{-3}$ s)
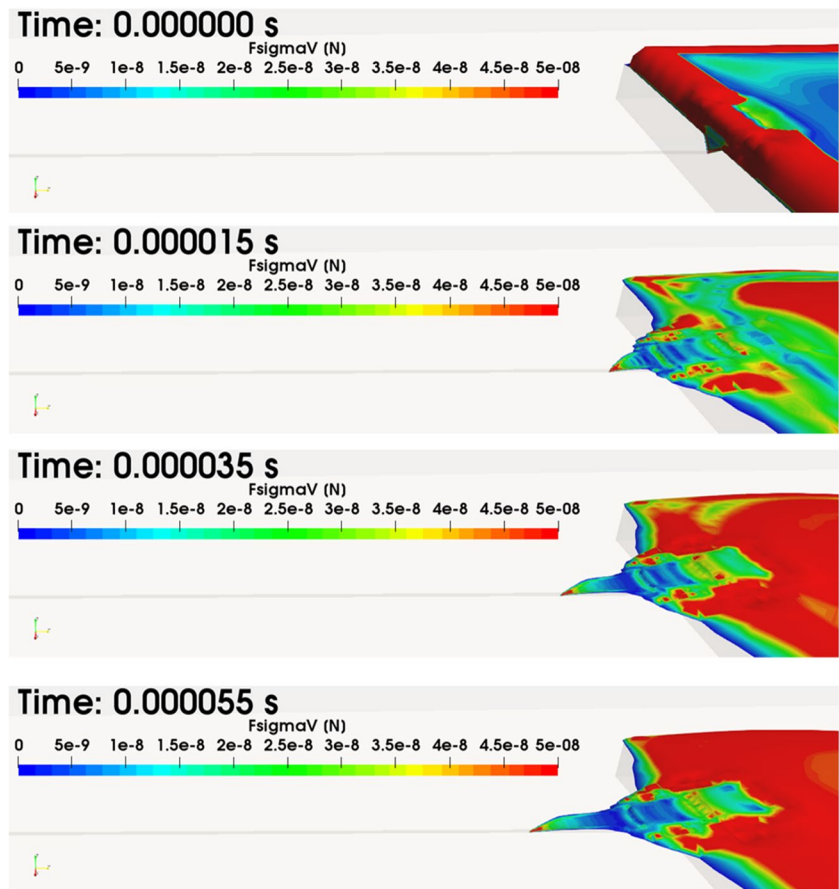
Time: 0.002000 s

Time: 0.002000 s          Uxz (m/s)
0   0.02 0.04 0.06 0.08  0.1  0.12 0.14 0.16 0.18  0.2

**Fig. 26** Velocity distribution of filler flow in the vertical section of the channel ($\theta_c = 15.5°$; channel groove no. 14; $t = 2.0 \times 10.^{-3}$ s)

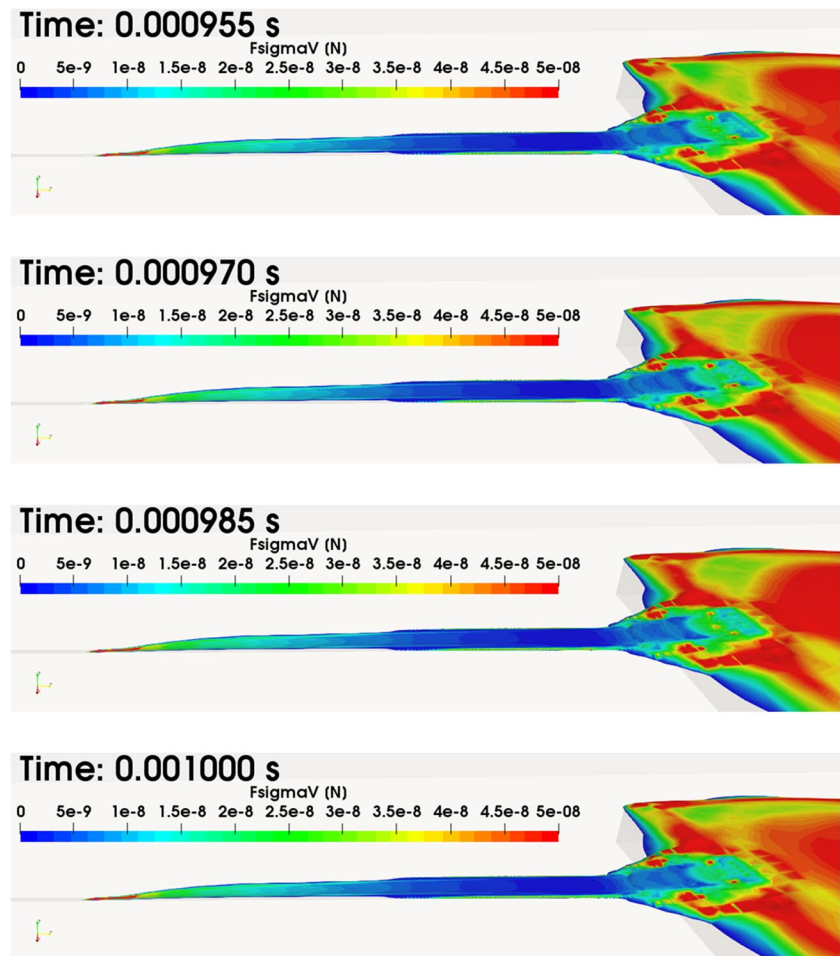**Fig. 27** Surface tension $F_s$ (no. 14; $\theta_c = 15.5°$; $t = 0.000000$–$0.000055$ s)

## 4.4 Analysis of filler flow

The obtained pressure and velocity distributions of the filler were used to examine its flow behavior in channel groove no. 14 with a contact angle of $\theta_c = 15.5°$. Figure 24 shows the pressure distribution of the filler flow, and Figs. 25 (horizontal section of channel groove) and 26 (vertical section of channel groove) show the velocity distributions.

For the initial filler flow at $t = 1.0 \times 10^{-5}$ s, the absolute value of the pressure was high at the pool and in the channel groove near the pool and decreased as the filler tip approached. The absolute value of the velocity was large from the pool to the channel groove.

For times $t = 1.0 \times 10^{-5}$ s and beyond, by which the flow had stabilized, the results show that the pressure was large near the pool and decreased as the filler tip approached. Compared with the pressure in the initial flow period, the pressure in the pool area decreased. The distribution of velocity vectors indicates that the filler flowed in the direction of not only the channel groove but also the pool and formed vortices near the boundary

Time: 0.000000 s
FsigmaV (N)
0   5e-9  1e-8 1.5e-8 2e-8 2.5e-8 3e-8 3.5e-8 4e-8 4.5e-8 5e-08

Time: 0.000015 s
FsigmaV (N)
0   5e-9  1e-8 1.5e-8 2e-8 2.5e-8 3e-8 3.5e-8 4e-8 4.5e-8 5e-08

Time: 0.000035 s
FsigmaV (N)
0   5e-9  1e-8 1.5e-8 2e-8 2.5e-8 3e-8 3.5e-8 4e-8 4.5e-8 5e-08

Time: 0.000055 s
FsigmaV (N)
0   5e-9  1e-8 1.5e-8 2e-8 2.5e-8 3e-8 3.5e-8 4e-8 4.5e-8 5e-08

between the pool and the channel. The filler fluid that flowed into the pool was classified into two types of behavior: (i) the brazing fluid returned toward the pool and merged into the vortex or (ii) it flowed directly into the channel groove without vortexing.

The flow of filler into the channel groove changes the shape of the meniscus of the filler in the pool, which is considered to generate tension in the pool, and the filler flowing into the channel groove is pulled into the pool, forming a vortex. However, because the tension decreases as the filler leaves the pool, the surface tension between the channel groove and the filler becomes dominant in the channel groove farther away from the pool, and the filler tip flows in the direction of the empty channel.

## 4.5 Force analysis (surface tension and wall shear stress)

The relationships among filler tip velocity $v_t$, surface tension $F_s$, and wall shear stress $\tau_w$ were examined for channel groove no. 14 with a contact angle of $\theta_c = 15.5°$. Figures 27 and 28 show the modeling results for $F_s$, and Figs. 29 and 30 show those for $\tau_w$.

The results for $F_s$ show that the surface tension that was distributed at the edge of the pool immediately after the start of the calculation then accumulated in the center of the pool. This was a temporary distribution until the meniscus shape in the pool section stabilized, and the time variation of the distribution in the pool section reached a steady state after $t = 3.5 \times 10^{-5}$ s. In contrast, the results for $t = 9.55 \times 10^{-3}$ s to $1.0 \times 10^{-3}$ s show that there was almost no change in the surface-tension distribution at the pool.

Next, the results for $\tau_w$ show that the absolute value of $\tau_w$ was concentrated at the tip of the filler at times $t = 0$ to $5.5 \times 10^{-5}$ s. However, at times $t = 9.55 \times 10^{-3}$ s to $1.0 \times 10^{-3}$ s, the concentrated high-value distribution of $\tau_w$ was not observed.

Figure 31 shows the time variations of the velocity $v_t$ of the filler tip, the wall shear stress $\tau_w$, and the surface tension $F_s$. The trends of each variable with time are

**Fig. 29** Wall shear stress
$\tau_w$ (no. 14; $\theta_c = 15.5°$;
$t = 0.000000$–$0.000055$ s)
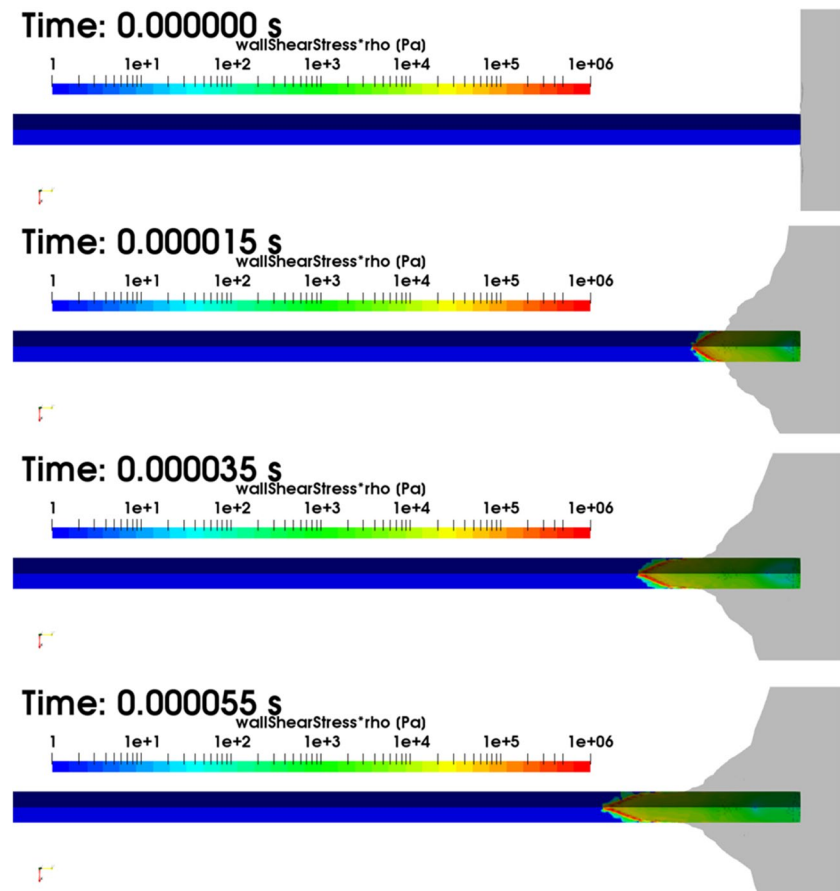


similar, with the values decreasing rapidly with time until approximately $5.0 \times 10^{-4}$ s, after which the rate of decrease became smaller.

These results suggest that the meniscus change at the interface between the molten filler and the ambient gas is the dominant driving force for surface-tension flow in the early stage of filler flow, and the unsteady surface-tension flow associated with the dynamic contact-angle change formed on the channel wall becomes dominant after that.

Figure 32 shows the relationship between filler tip velocity and wall shear stress, and Fig. 33 shows the relationship between filler tip velocity and surface tension. Both the wall shear stress and surface tension have a direct relationship with filler tip velocity, and the slope decreases as the velocity increased. From the previous discussion about the time variations of surface tension and wall shear stress, the unsteady surface-tension flow due to the dynamic contact-angle change formed between the filler and the channel wall is dominant at low velocity, whereas for high velocity, the slope is considered to have changed because of the additional effect

of surface-tension flow due to the meniscus change, in addition to the effect of dynamic contact-angle change.

Figure 34 shows a linear relationship between surface tension and wall shear stress. As the driving force from surface tension increased, so did the frictional force (wall shear stress), and we could examine the relationship quantitatively.

### 4.6 Effects of various parameters on filler flow

#### 4.6.1 Initial shape and gravity

The effects of the initial shape and gravity on filler flow were examined. Figure 35 shows the initial shape of the filler. Numerical analyses were performed for the following cases: (i) the meniscus was considered in the initial condition (initial meniscus), (ii) the meniscus was not considered in the initial condition (initial box shape), and (iii) the meniscus was not considered in the initial condition and gravity was zero (initial box + zero gravity). The geometry of channel groove no. 14 was used.

**Fig. 30** Wall shear stress $\tau_w$ (no. 14; $\theta_c = 15.5°$; $t = 0.000955$–$0.001000$ s)
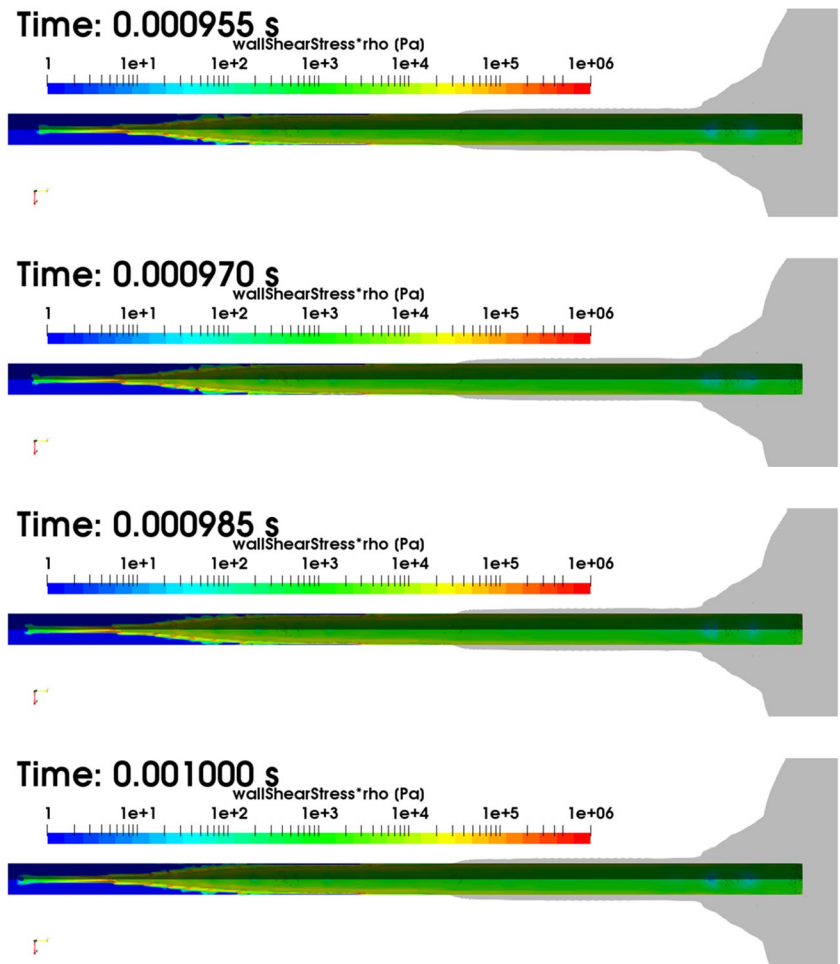


Figure 36 shows the instantaneous behavior of the filler, and Fig. 37 shows the time evolution of the filler tip position. Comparing the three calculated conditions, there is almost no difference in the time evolution of the filler tip position. This indicates that the effects of the initial shape and gravity on the flow behavior of the filler tip in the channel groove are negligible.
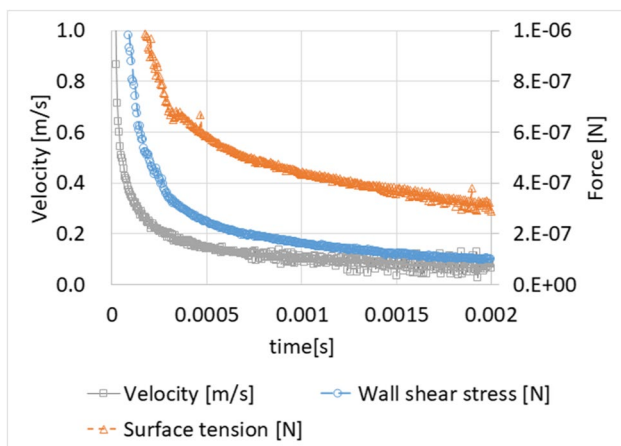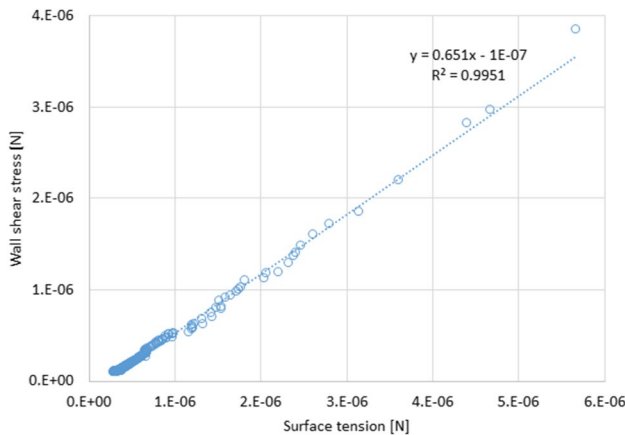


**Fig. 31** Velocity $v_t$ of the filler tip, wall shear stress $\tau_w$, and surface tension $F_s$
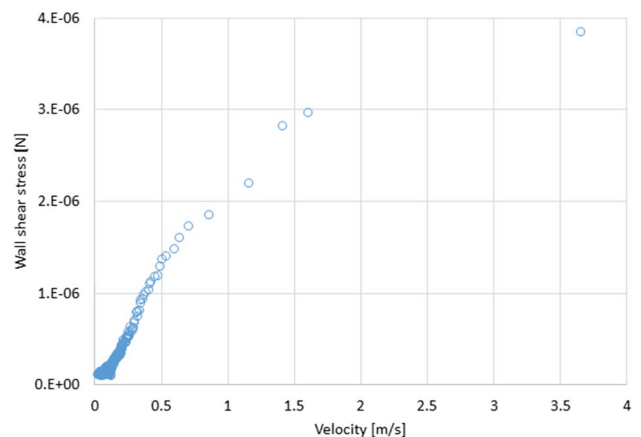


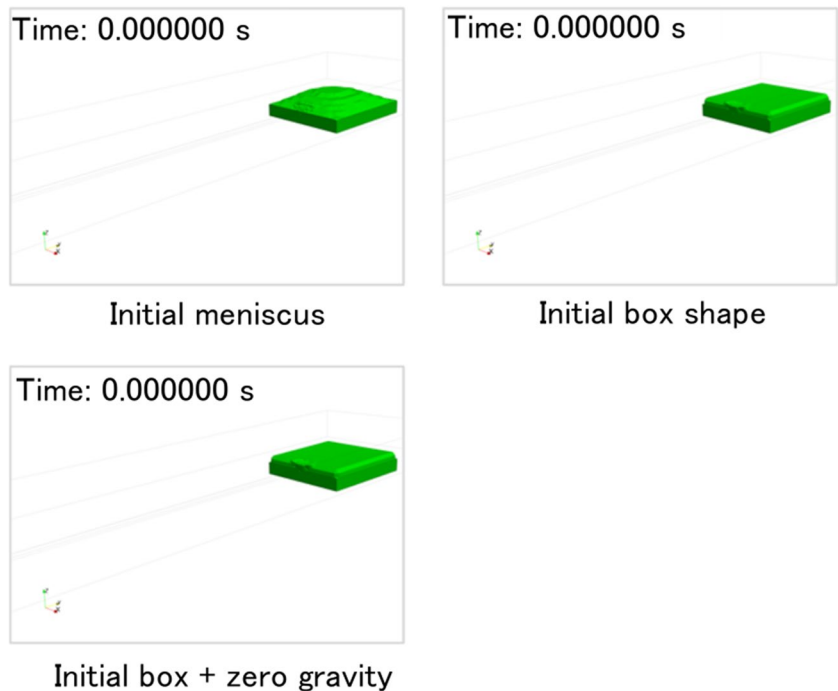**Fig. 32** Velocity $v_t$ of the filler tip and wall shear stress $\tau_w$ (channel groove no. 14; $\theta_c = 15.5°$)
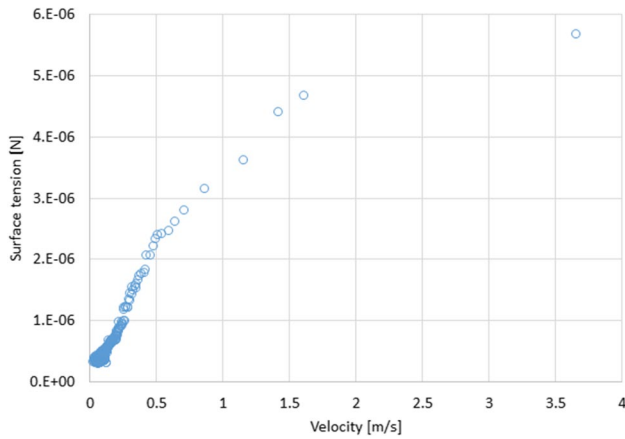
**Fig. 33** Velocity $v_t$ of the filler tip and surface tension $F_s$ (channel groove no. 14; $\theta_c = 15.5°$)



**Fig. 34** Surface tension $F_s$ and wall shear stress $\tau_w$ (channel groove no. 14; $\theta_c = 15.5°$)

**Fig. 35** Initial shape (initial meniscus, initial box shape, initial box shape + zero gravity; $t = 0.000000$ s)

### 4.6.2 Surface tension

To assess the effect of surface tension on filler flow, a numerical analysis was performed with the surface tension set to zero. Groove no. 14 was used, and the initial condition was calculated without considering the initial meniscus (i.e., the initial box shape).

Figure 38 shows the instantaneous filler behavior, and Fig. 39 shows the position of the filler tip as it changes with time. With zero surface tension, the position of the filler tip did not change with time. This indicates that no filler flows through the groove when the surface tension is extremely low.

### 4.6.3 Viscosity

To assess the effect of viscosity on filler flow, numerical analyses were conducted with kinematic viscosities of $\mu$, $\mu/2$, and $2\mu$ (for $\mu = 6.62249 \times 10^{-6}$ m$^2$/s). Groove no. 14 was used, and the initial condition was calculated without considering the initial meniscus (i.e., the initial box shape).

Figure 40 shows the instantaneous filler flow, and Fig. 41 shows the time variation of the filler tip position. Compared with that for kinematic viscosity $\mu$, the movement distance of the filler was approximately 30% greater with $\mu/2$ and approximately 30% less with $2\mu$. This indicates that viscosity affects the filler tip velocity. Notably, the viscosity of the Al-Si alloy material decreases as the temperature increases,



Initial meniscus



Initial box shape



Initial box + zero gravity

**Fig. 36** Instantaneous filler flow (initial meniscus, initial box shape, initial box shape + zero gravity; $t = 0.002000$ s)



Initial meniscus



Initial box shape



Initial box + zero gravity
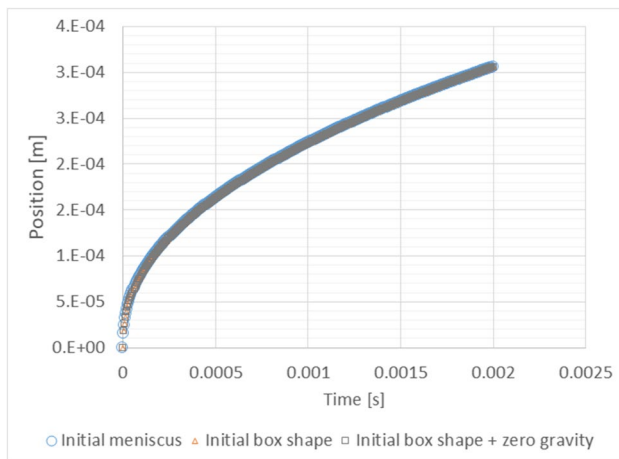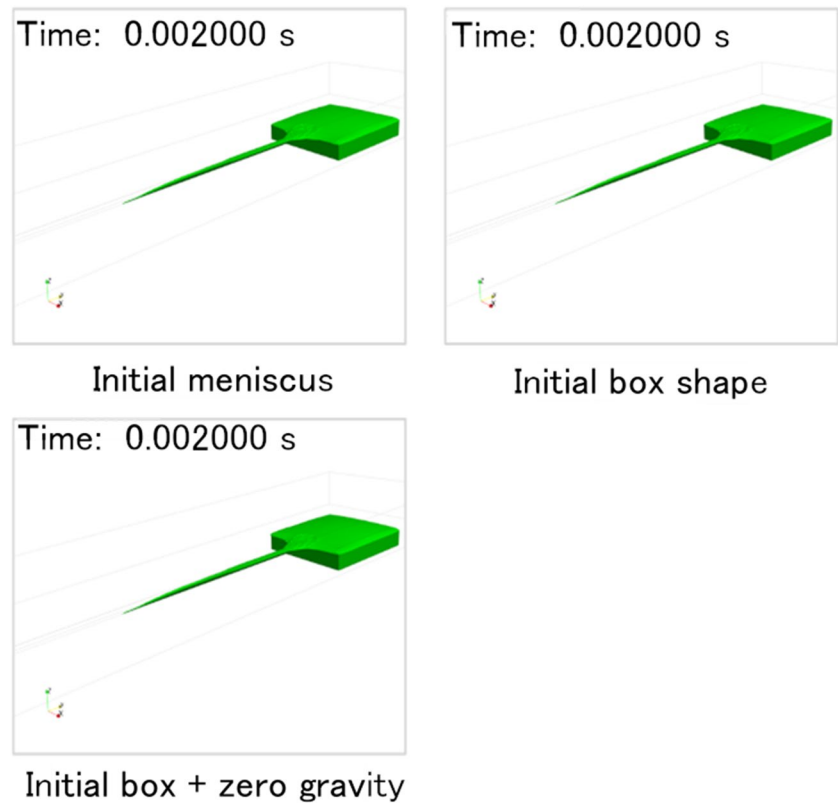


**Fig. 37** Filler tip position (initial meniscus, initial box shape, initial box shape + zero gravity)

suggesting that the filler-flow rate increases as the brazing temperature increases.

### 4.6.4 Boundary conditions

To assess the effect of shear stress between the channel wall surface and filler fluid, numerical analyses were conducted with (no slip) and without (slip) shear stress. Channel groove no. 14 was used, and the initial condition was calculated without considering the initial meniscus (i.e., the initial box shape).

Figure 42 shows the instantaneous behavior of the filler, and Fig. 43 shows the time variation of the filler tip position. Compared with that in the condition of applied shear stress (no slip), the filler tip movement increased approximately 36-fold without the applied shear stress (slip). This velocity is much higher than the experimental values and is presumed to differ from the actual phenomenon, which suggests that the effect of shear stress cannot be ignored. The no-slip condition, in which shear stress exists, is necessary for the numerical analysis of filler flow in a groove.
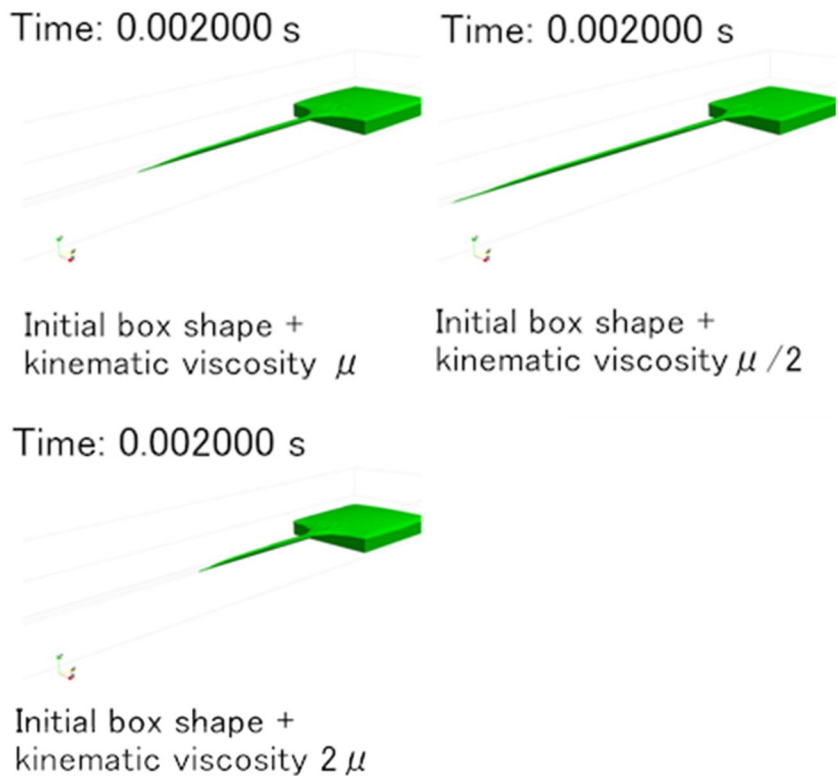
## 5 Conclusions

This study is aimed at clarifying the surface-tension flow mechanism of molten filler, and a numerical study of the surface-tension flow in microgrooves was conducted. Specifically, the surface-tension flow behavior was analyzed by simulating various cross-sectional shapes of the

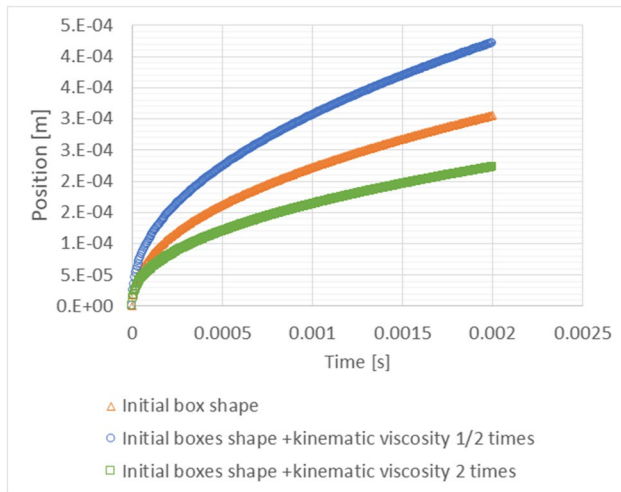**Fig. 38** Instantaneous filler flow (with and without surface tension)

Time: 0.002000 s　　　　　Time: 0.002000 s

Initial box shape　　　　　Initial box shape + zero surface tension
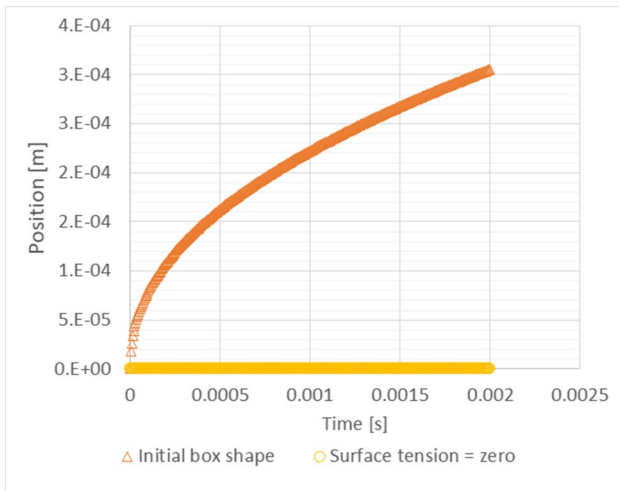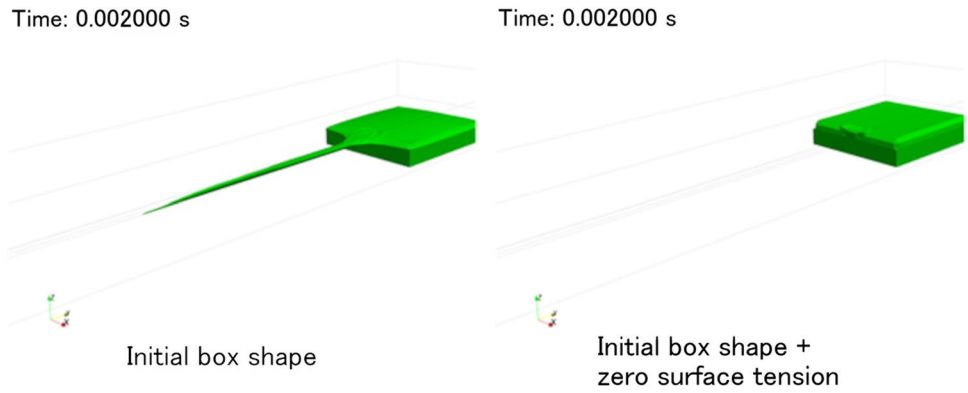


**Fig. 39** Filler tip position (with and without surface tension)

channel grooves and various contact angles of the filler. The effects of various parameters, such as viscosity and boundary conditions, on the filler flow were also analyzed. The results obtained from this study are summarized below.

1) In a microgroove, when the contact angle of the filler fluid is below a specific value, the surface tension acting on the groove becomes dominant, and filler flow occurs. The filler-flow velocity increases as the contact angle of the filler decreases

2) The filler velocity increases as the channel groove width decreases or the channel groove depth increases. In other words, the capillary force that dominates the filler surface-tension flow in the

**Fig. 40** Instantaneous filler flow (kinematic viscosities $\mu$, $\mu/2$, and $2\mu$ for $\mu = 6.62249 \times 10^{-6}$ m.$^2$/s)

Time: 0.002000 s　　　　　Time: 0.002000 s

Initial box shape + kinematic viscosity $\mu$　　　　　Initial box shape + kinematic viscosity $\mu/2$

Time: 0.002000 s

Initial box shape + kinematic viscosity $2\mu$

**Fig. 41** Filler tip position (kinematic viscosities $\mu$, $\mu/2$, and $2\mu$ for $\mu = 6.62249 \times 10^{-6}$ m.$^2$/s)
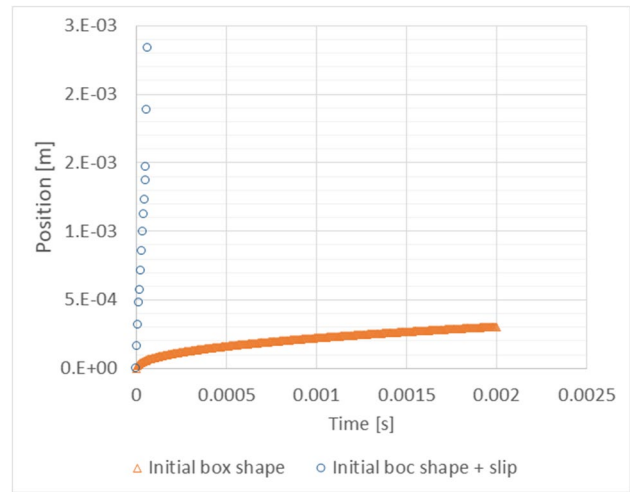


**Fig. 43** Time variation of filler tip position (no slip vs. slip)

groove is highly dependent on the groove width and depth. The surface curvature of the filler increases with decreasing groove width or increasing groove depth, and the increased capillary force promotes the surface-tension flow of the filler in the groove

3) When the cross-sectional area of the channel groove increases, the filler-flow velocity increases, and the rate of unsteady fluctuation increases with the increasing filler tip velocity. The driving force of the filler flow in the channel groove is considered to be (i) the surface tension, which is based on the filler free-surface curvature, or (ii) the dynamic change in the shape of the meniscus, which can be unsteady and induced by Rayleigh–Taylor instability. As the cross-sectional area of the channel groove increases, the capillary force based on the dynamic change in the meniscus shape of the flowing filler in the groove dominates the unsteady change in filler tip velocity,

rather than the surface tension based on the filler free-surface curvature formed in the groove

4) The filler fluid flow behavior is classified into two types: (i) the filler fluid merges into the vortex formed by the backflow of filler toward the pool, and (ii) the filler fluid flows directly into the channel groove without vortexing. The filler flow into the channel groove generates an interfacial tension based on the change in the shape of the filler fluid meniscus in the pool. This tension generates a pulling force in the direction of the pool, causing the filler fluid to flow back into the pool and form vortices. However, because the tension in the pool decreases with increasing distance from the pool, the surface tension acting on the filler fluid in the channel becomes dominant in the channel groove farther away from the pool, and the filler tip flows in the direction of the empty channel

5) The unsteady filler flow behavior was analyzed. The change in meniscus shape at the interface between the filler and ambient gas acts as the dominant driving force in the surface-tension flow during the

**Fig. 42** Instantaneous filler flow (no slip vs. slip)
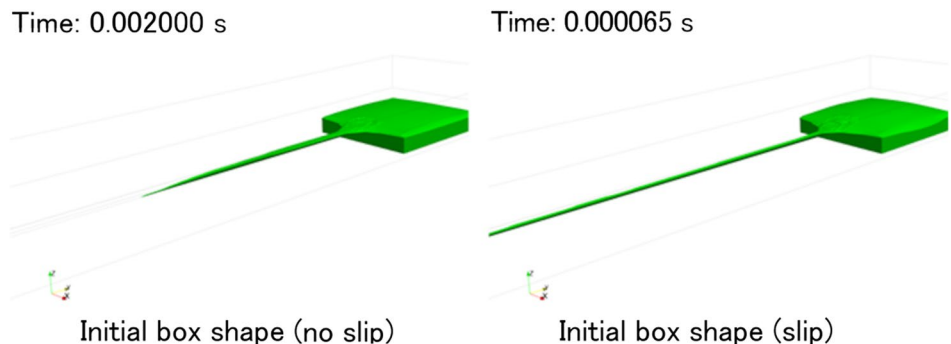
initial stage. Then, unsteady surface-tension flow associated with the dynamic contact-angle change becomes dominant. At low velocity, unsteady surface-tension flow associated with the dynamic contact-angle change is dominant, but at high velocity, the effect of surface-tension flow due to the change in meniscus shape is added to the effect of the dynamic contact-angle change

6) A linear relationship has been clarified between surface tension and wall shear stress. Additionally, the fluid friction force based on the wall shear stress becomes the dominant driving force owing to the increase in surface tension.

Future developments in erosion estimation require numerical models incorporating the filler temperature and groove decomposition.

**Nomenclature** $t$: Time; $U$: Mixture velocity; $P$: Mixture pressure; $\alpha$: Volume fraction of the liquid phase; $\rho$: Density of the mixture; $\mu$: Viscosity coefficient of mixture; $\mu^{\text{eff}}$: Effective viscosity of the mixture; $\mu^t$: Turbulent viscosity of the mixture; $g$: Acceleration due to gravity; $\tau$: Viscous stress tensor; $F_s$: Force source term due to surface tension; $n$: Unit vector of the interface; $k$: Interfacial curvature; $\sigma$: Interfacial surface tension

**Author contribution** Hiroshi Otsuki and Jun Ishimoto developed and validated the proposed method. All authors analyzed the results and approved the final manuscript.

## Declarations

**Conflict of interest** The authors declare no competing interests.

## References

1. Khorunov VF, Sabadash OM (2013) 9-Brazing of aluminum and aluminum to steel. Adv Braz 249–279. https://doi.org/10.1533/9780857096500.2.249

2. Benoit MJ, Han KB, Winkler S, Worswick MJ, Wells MA (2019) An assessment of the brazing performance of warm formed automotive heat exchangers. Int J Adv Manuf Technol 103:1935–1946

3. Dong Y, Zhang C, Luo W, Yang S, Zhao G (2016) Material flow analysis and extrusion die modifications for an irregular and multitooth aluminum alloy radiator. Int J Adv Manuf Technol 85:1927–1935

4. Tanner LH (1978) Spreading of silicone oil drops on horizontal surface. J Phys D 12:1473–1484

5. Wittebrood A, Bürger A, Kirkham S (2011) Flux free brazing of aluminium heat exchangers. Vehicle Thermal Management Systems Conference and Exhibition (VTMS10), pp 35–43. https://doi.org/10.1533/9780857095053.2.35

6. Zhao H, Woods R (2013) 10-Controlled atmosphere brazing of aluminum. AdvBraz 280–322 https://doi.org/10.1533/9780857096500.2.280

7. Sekulić DP (2013) 3-Modeling of the sequence of phenomena in brazing. Adv Braz 55–81. https://doi.org/10.1533/9780857096500.1.55

8. Cui XL, Wang XS, Yuan SJ (2017) Formability improvement of 5052 aluminum alloy tube by the outer cladding tube. Int J Adv Manuf Technol 90:1617–1624

9. Tsao LC (2002) Brazeability of a 3003 aluminum alloy with Al-Si-Cu-based filler metals. J Mater Eng Perform 11:360–364

10. Terrill JR (1966) Diffusion of silicon in aluminum brazing sheet. Weld J Res Suppl 45(5):202–209

11. Nylén M et al (2000) The mechanism of braze metal penetration by migration of liquid films in aluminum. Mater Sci Forum 331–337:1737–1742

12. Izumi T (2016) Influence of erosion phenomenon on flow behavior of liquid Al-Si filler between brazed components. ICAA13 Pittsburgh

13. Nylén M et al (2002) Mechanisms of erosion during brazing of aluminum alloys. Mater Sci Forum 396–402:1585–1590

14. Zhao H, ElbelS, Hrnjak P (2014) Influence of surface morphology on wetting behaviors of liquid metal during aluminum heat exchanger fabrication. 15th International Refrigeration and Air Conditioning Conference at Purdue

15. Mirski Z, Pabian J, Wojdat T (2021) Dissolution and erosion phenomena in the brazing of aluminum heat exchangers. Arch Metall Mater 66(4):1131–1140

16. Ito Y, Namba K (1989) Erosion in aluminum brazing. Sumitomo Light Metal Tech 30(2):53–63

17. Lacaze J (2018) Numerical simulation of brazing aluminium alloys with Al–Si alloys. Trans Indian Inst Met 71:2623–2629

18. Murase T, Yanagawa Y (2009) Effects of liquid filler metal and base metal composition on erosion characteristics during aluminum brazing. J Light Met Weld 47(1):18–25. https://doi.org/10.11283/jlwa.47.18

19 Washburn EW (1921) The dynamics of capillary flow. Phys Rev 17:273–283

20. Yost FG, Rye RR, Mann JA Jr (1997) Solder wetting kinetics in narrow V-grooves. Acta Mater 45:5337–5345. https://doi.org/10.1016/S1359-6454(97)00205-X

21. Teshima S, Ogawa H (2007) Denso technical review. 12(2):144–150

22 Zhao H, Sekulic DP (2008) Wetting kinetics of a hypo-eutectic Al–Si system. Mater Lett 62(15):2241–2244. https://doi.org/10.1016/j.matlet.2007.11.081

23. Fu H, Dehsara M, Krivilyov M, Mesarovic SD, Sekulic DP (2016) Kinetics of the molten Al–Si triple line movement during a brazed joint formation. J Mater Sci 51:1798–1812. https://doi.org/10.1007/s10853-015-9550-7

24. Tanaka H (2021) Numerical analysis of fillet shape and molten filler flow during brazing in the Al–Si alloy of automotive radiator.

Mater Trans 62(4):498–504. https://doi.org/10.2320/matertrans.L-M2020874

25. Zhao H, Stefan ELBEL, Pega HRNJAK (2021) Low melting temperature brazing materials for aluminum heat exchanger fabrication. 18th International Refrigeration and Air Conditioning Conference at Purdue

26. Sekulic DP (2001) Molten aluminum equilibrium membrane formed during controlled atmosphere brazing. Int J Eng Sci 39:229–241. https://doi.org/10.1016/S0020-7225(00)00022-7

27. Zellmer BP, Nigro N, Sekulic DP (2001) Numerical modelling and experimental verification of the formation of 2D and 3D brazed joints. Modell Simul Mater Sci Eng 9:339–355. https://doi.org/10.1088/0965-0393/9/5/301

28. Seklic DP et al (2004) Prediction of the fillet mass and topology of aluminum brazed joints. Weld J 83(3):102s–110s

29. Eustathopoulos N, Hodaj F, Kozlova O (2013) 1 - The wetting process in brazing. Adv Braz 3–30. https://doi.org/10.1533/9780857096500.1.3

30. Way M, Willingham J, Goodall R (2020) Int Mater Rev 65(5):257–285

31. Narumi Y, Ishimoto J, Kanayama D, Kuribara H, Nakano Y (2022) Computational fluid–structure interaction analysis of piston pin multiphase elastohydrodynamic lubrication with unsteady flow channel variation. ASME J Tribol 145(2):021603. February 2023. https://doi.org/10.1115/1.4055407

32. Ishimoto J, Shimada S (2022) Coupled computing for reactive hydrogen leakage phenomena with crack propagation in a pressure tank. Int J Hydrogen Energy 47(4):2735–2758. https://doi.org/10.1016/j.ijhydene.2021.10.167

33. Ishimoto Jun, Sato F, Sato G (2010) Computational prediction of the effect of microcavitation on an atomization mechanism in a gasoline injector nozzle. ASME J Eng Gas Turbines Power 132(8):082801. https://doi.org/10.1115/1.4000264

34. Shichang Xu (2022) Numerical modeling of coupled arc plasma, metal transfer and molten pool evolution for underwater flux-cored arc welding. Int J Adv Manuf Technol 123:2605–2622

35. Ren X (2023) Comparison of LES and RANS simulation on turbulent round jet. Int J Adv Manuf Technol

36. Cao Liu (2018) Prediction of gas entrapment defects during zinc alloy high-pressure die casting based on gas-liquid multiphase flow model. Int J Adv Manuf Technol 94:807–815

37. Yakovenko SN (2011) Application of the continuum surface force model to the Rayleigh — Taylor instability problem. Thermophys Aeromechanics 18:433–445